Terahertz Light Sources by Electronic-Oscillator-Driven Second-Harmonic Generation in Cavities Featuring Extreme Confinement

Hyeongrak Choi, Lamia Ateshian, Mikkel Heuck, and Dirk Englund

Phys. Rev. Applied **18**, 044019 — Published 7 October 2022

DOI: 10.1103/PhysRevApplied.18.044019

Terahertz light sources by electronic-oscillator-driven second harmonic generation in extreme-confinement cavities

Hyeongrak Choi,[1, 2, *] Lamia Ateshian[1, 2, ‡], Mikkel Heuck[1, 2], and Dirk Englund[1, 2, †]

[1] *Research Laboratory of Electronics, Massachusetts Institute of Technology, Cambridge, Massachusetts 02139, USA*
[2] *Department of Electrical Engineering and Computer Science, Massachusetts Institute of Technology, Cambridge, Massachusetts 02139, USA*

(Dated: September 9, 2022)

The majority of sources of coherent optical radiation rely on laser oscillators driven by population inversion. Despite their technological importance in communications, medicine, industry, and other fields, it remains a challenge to access the spectral range of 0.1-10 THz (the "terahertz gap"), a frequency band for applications ranging from spectroscopy to security and high-speed wireless communications. Here, we propose a way to produce coherent radiation spanning the THz gap by efficient second-harmonic generation (SHG) in low-loss dielectric structures, starting from technologically mature electronic oscillators (EOs) in the ∼100 GHz range. To achieve this goal, we introduce hybrid THz-band dielectric cavity designs that combine (1) extreme field concentration in high-quality-factor resonators with (2) nonlinear materials enhanced by phonon resonances. We theoretically predict conversion efficiencies of $> 10^3$%/W and the potential to bridge the THz gap with 1 W of input power. This approach enables efficient, cascaded parametric frequency converters, and light sources extensible into the mid-IR spectrum and beyond.

I. INTRODUCTION

There are fundamental differences in how frequency-stable electromagnetic (EM) radiation is generated at frequencies $\omega/2\pi \ll 1$ THz and $\omega/2\pi \gg 1$ THz. The majority of sub-THz sources rely on electronic oscillators (EOs) or frequency multipliers. Far above ∼10 THz, sources use gain media based on population inversion. Separating these frequency regimes is the "THz gap," commonly defined as 0.1 - 10 THz, in which efficient, compact, and room-temperature EM sources have been notoriously challenging to build. However, the abundance of opportunities in the THz spectrum for a range of applications – from molecular spectroscopy to remote sensing, navigation, and wireless communication [1–3] – motivates the development of more efficient sources in this band. Within the THz gap (Fig. 1(a)) sources based on electronic methods are possible through nonlinear electrical frequency-multipliers and high-frequency oscillators. Passive frequency-multipliers typically have an efficiency scaling of $1/N^2$ $(1/N)$ for the N^{th} harmonic when they are operated in resistive (reactive) regime, for example, by forward (reverse) biasing Schottky diodes. On the other hand, active multipliers such as GaAs MESFET, Si MOSFET, InP HEMT, and SiGe HBT require DC power consumption [4]. All in all, their operation becomes inefficient above the maximum operational frequency of transistors $f_{max} \sim 100 - 300$ GHz [2, 4]. On the other hand, THz sources derived from population inversion have low efficiencies (e.g. 0.02% for optical DFG [5]), require cryogenic cooling (e.g. quantum-cascade lasers [6]), or rely on expensive and bulk ultra-fast lasers [7].

Here, we introduce an approach based on extreme field concentration with high quality factor cavities [8, 9] that achieves frequency conversion from ∼ 100 GHz (microwave) into the THz domain with efficiencies exceeding 10^3 %/W. Our approach opens the door to efficient, phase-stable synthesis of electromagnetic radiation bridging the terahertz gap.

As indicated in Fig. 1(a), we consider an electronic source at the low end of the THz gap that drives the first stage of second-harmonic generation (SHG) in a dielectric cavity. This cavity is made of a low-loss dielectric material that creates a deep sub-wavelength region of high electric energy density inside a $\chi^{(2)}$ nonlinear material. After the first conversion step (ω_a to $\omega_b = 2\omega_a$), the output is injected into the next cavity. After cascading N cavities, the output frequency is $2^N\omega_a$. The absence of a gain medium eliminates numerous challenges such as quantum noises (spontaneous emission) and technical noises (drive current noise, relaxation oscillations, vibrations, etc), promising phase-stability inherited from the electronic seed oscillator.

The efficiency of the SHG approach increases with the pump power and is only limited by the dielectric breakdown of materials. Because the SHG is "parametric" (which does not dissipate power), our SHG approach mitigates the sharp efficiency drop in electronic sources above f_{max} due to ohmic losses and other parasitic losses of nonlinear reactances [4]. Figure 1(a) plots the estimates of the resulting output power at each stage of the SHG cascade with a 400 mW, 1 W, and 4 W input. Further advances in EO output power, cavity designs, and nonlinear materials should further increase the efficiency spanning the entire THz gap.

Figure 1(b) illustrates the SHG cascade using a doubly-resonant photonic crystal (PhC) cavity. Pumping mode a with a power P_p generates a field in mode b with efficiency

* choihr@mit.edu
‡ H.C. and L.A. equally contributed to this work.
† englund@mit.edu

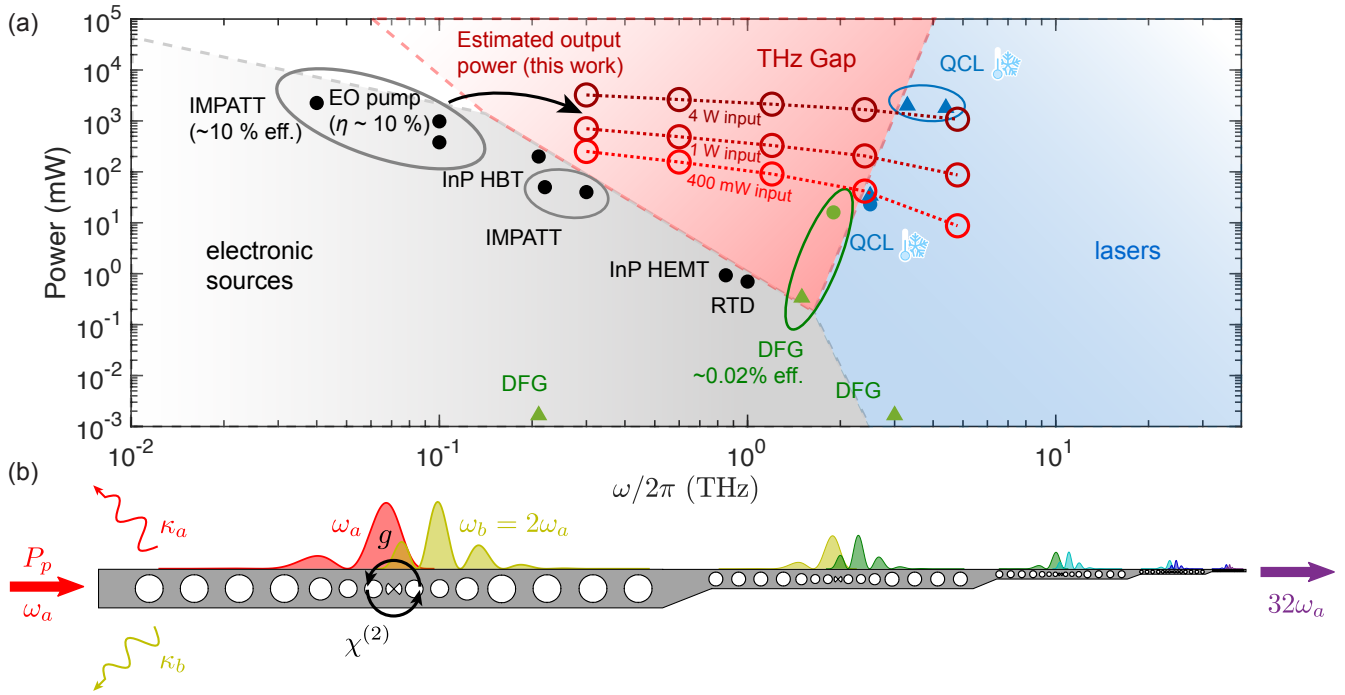

FIG. 1. Terahertz sources and proposed work. (a) Selected terahertz source technologies [10] based on electronics (black), lasers (blue), and difference frequency generation (DFG) in nonlinear crystals (green) [5, 11–20]). "Terahertz gap" is shaded in red; available output power in 100 GHz - 10 THz range is limited. Approximate wall-plug efficiency is indicated where available. Circles denote CW power and triangles denote average pulse power. Our proposed device (results for ring cavity shown here) starts with an EO input at ∼1 W, ∼100 GHz (circled) to generate output power crossing the THz gap by cascaded frequency doubling. For comparison, output power for 400 mW and 4 W input power are also shown. In this calculation, we included the radiation loss of the SH cavity mode and neglected direct radiation loss from the nonlinear polarization field into other modes at the SH frequency (see Appendix A). (b) Schematic of spectrum-spanning nonlinear frequency synthesis approach in PhC cavities. The fundamental mode at ω_a is coupled to the second-harmonic mode at $\omega_b = 2\omega_a$ in the first cavity with coupling rate g. The output at ω_b couples to the next cavity, cascading in a sequence of frequency doubling steps. After N steps the final output is at $2^N\omega_a$ (here $N = 5$).

η_{SHG} (see Appendix A)

$$\eta_{\mathrm{SHG}} \equiv \frac{P_{\mathrm{SHG}}}{P_p^2} = \frac{64}{\hbar\omega_a^4} g^2 Q_a^2 Q_b \eta_c, \tag{1}$$

where η_c is the input-output coupling efficiency, Q_a and Q_b are the quality factors of the fundamental (FD) and second-harmonic (SH) modes, respectively, and g is the nonlinear coupling rate, given by

$$g = \chi^{(2)}_{\mathrm{eff}} \sqrt{\frac{\hbar\omega_a^2\omega_b}{\epsilon_0}} \frac{\tilde{\beta}}{\sqrt{(\lambda_a/n_a)^3}}, \tag{2}$$

where $\chi^{(2)}_{\mathrm{eff}}$ is the effective second-order nonlinear coefficient, n_a is the refractive index of the nonlinear material at ω_a, and $\tilde{\beta}$ is the SHG mode overlap between the FD and SH modes, normalized to the wavelength in the nonlinear medium.

Considering $\omega_b, 1/\lambda_a \propto \omega_a$, the coupling rate g is proportional to ω_a^3, and thus, $\eta_{\mathrm{SHG}} \propto \omega_a^2$. The dependence of the conversion efficiency on the frequency squared poses a technical challenge in THz SHG compared to its optical counterpart. We will show that this scaling can be overcome with a combination of (1) materials with large nonlinear coefficient derived from phonon resonances and (2) cavity designs with strong field confinement.

II. NONLINEAR MATERIAL ANALYSIS

We make use of large second-order nonlinear susceptibilities derived from transverse optical (TO) phonon resonances. Transverse optical phonons can be driven by EM waves, resulting in large linear susceptibilities. The nonlinear susceptibilities are higher on resonance because they are proportional to the linear susceptibilities at the frequency components of interest [21]. Phonon resonance frequencies lie at several THz for the crystals we consider here: GaAs, GaP, and ZnTe (zinc-blendes, class $\bar{4}3m$); and $LiTaO_3$ and $LiNbO_3$ (ferroelectrics, class $3m$).

Since experimental data on THz nonlinear optical susceptibilities in materials are limited, we rely on theoretical models supported by the existing data. The Faust-Henry model [22, 23] is used for zinc-blende crystals and an extension of Miller's rule [24] for ferroelectric crys-

tals. In both models, nonlinear coefficients are expressed by products of Lorentzian oscillators. (Details of the calculations of nonlinear susceptibilities can be found in Appendix B.)

The dispersion of the linear susceptibility $\chi^{(1)} = \epsilon - 1 = (n - \frac{ic\alpha}{2\omega})^2 - 1$ (where ϵ is the relative permittivity) is calculated by the damped oscillator model. The refractive index, n, and absorption coefficient, α, are plotted in Figs. 2(a) and (b). Parameters used in the calculations (e.g., TO phonon frequencies, damping constants, and oscillator strengths) can be found in Table III in Appendix B and Refs. [25–32]. We note that although the theoretical prediction of the absorption coefficient goes to 0 as $\omega \to 0$, experiments using THz time-domain spectroscopy show appreciable absorption at low frequencies due to other dissipation processes not included in this model [26, 33–35].

Fig. 2(c) plots $|\chi^{(2)}(\omega, \omega, 2\omega)|$ as a function of the fundamental frequency from 0 to 10 THz. In the zinc-blende materials, the nonzero components of the nonlinear tensor $\chi^{(2)}_{14}$, $\chi^{(2)}_{25}$, and $\chi^{(2)}_{36}$ are all equal. For the ferroelectric crystals, $\chi^{(2)}_{33}$ and $\chi^{(2)}_{31}$ are shown.

Our calculations indicate that these phonon resonances result in remarkably high THz nonlinear susceptibilities for $LiTaO_3$ and $LiNbO_3$ of over 10^4 pm/V, exceeding their values in the optical range by around three orders of magnitude ($\chi^{(2)}_{33} = -40$ and -60 pm/V, respectively [21, 36]). GaAs, GaP, and ZnTe also show an order of magnitude increase relative to their optical counterparts ($\chi^{(2)}_{14} = 268, 156$, and 139 pm/V, respectively [29, 36]).

Early measurements of $\chi^{(2)}(\omega, \omega, 2\omega)$ at THz frequencies in GaAs and $LiTaO_3$ [26] provide a few experimental data points that agree with our calculated predictions. Follow-up work in GaAs additionally observed the resonant enhancement of SHG at half the phonon energy [25].

The large $\chi^{(2)}$ coefficients are accompanied by high absorption losses, as shown in Fig. 2(b). As such, standard cavity designs using a single material do not benefit from the $\chi^{(2)}$ due to the strong linear absorption. To overcome the loss, we introduce hybrid cavity designs in which the nonlinear materials are embedded in a low-loss dielectric, e.g., high-resistivity Si (see Appendix C 6).This allows us to take advantage of the $\chi^{(2)}$ while minimizing material losses.

We note that while the nonlinear optical properties of solids may be calculated more accurately from first principles through, e.g. density functional theory and bond charge models [37–41], such calculations are typically computationally expensive. The classical phenomenological models have been proven useful in estimating and fitting experimental data. Since the overall conversion efficiency of the device separately depends on material and geometric factors, discrepancies in the estimate of $\chi^{(2)}$ can be offset by modified cavity designs. Furthermore, phase matching only requires accurate estimates of the refractive index, which have been well-studied by experiments. In practice, thermal or electro-optic tuning may be used to correct for fabrication imperfections.

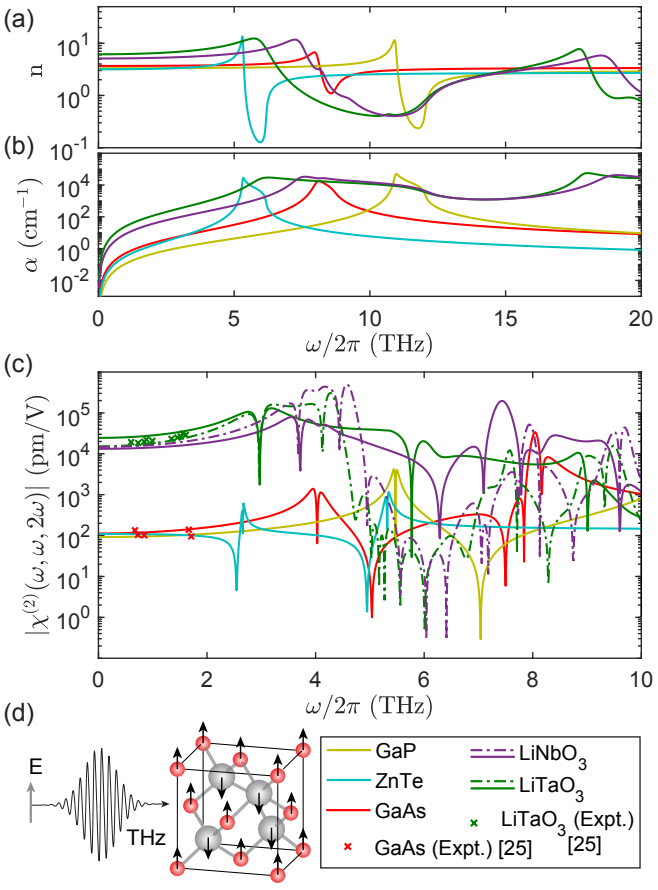

FIG. 2. Susceptibilities predicted from the theoretical models along with experimental data. (a) Refractive index (n_e for $LiTaO_3$ and $LiNbO_3$). (b) Absorption coefficient. (c) Second-order susceptibility, $|\chi^{(2)}_{jkl}(\omega, \omega, 2\omega)|$. Solid (using contracted notation): $\chi^{(2)}_{33}$ ($LiTaO_3$, $LiNbO_3$) or $\chi^{(2)}_{14}$ (GaAs, GaP, ZnTe). Dashed: $\chi^{(2)}_{31}$ ($LiTaO_3$, $LiNbO_3$). $\chi^{(2)}$ is plotted over half the frequency range of n and α since SHG from ω_a to $2\omega_a$ depends on n and α at both frequencies. Crosses indicate available experimental data [26]. (d) Illustration of transverse optical phonon mode excited by an incident THz field. When either the fundamental or second harmonic mode lies near the TO phonon frequency, the nonlinear susceptibility rapidly rises due to the resonance. The first maximum appears at half the lowest TO phonon frequency, for example, at ~ 4.0 THz in GaAs. A second peak occurs at $\omega_{TO} \sim 8.0$ THz, coinciding with the resonant features in the index and absorption coefficient in (a) and (b). Note that on resonance, the $\chi^{(2)}$ estimation can deviate. $\chi^{(2)}$ at 2.6 THz for ZnTe and at 5.2 THz for GaAs, ZnTe, $LiTaO_3$, and $LiNbO_3$ corresponds to this regime.

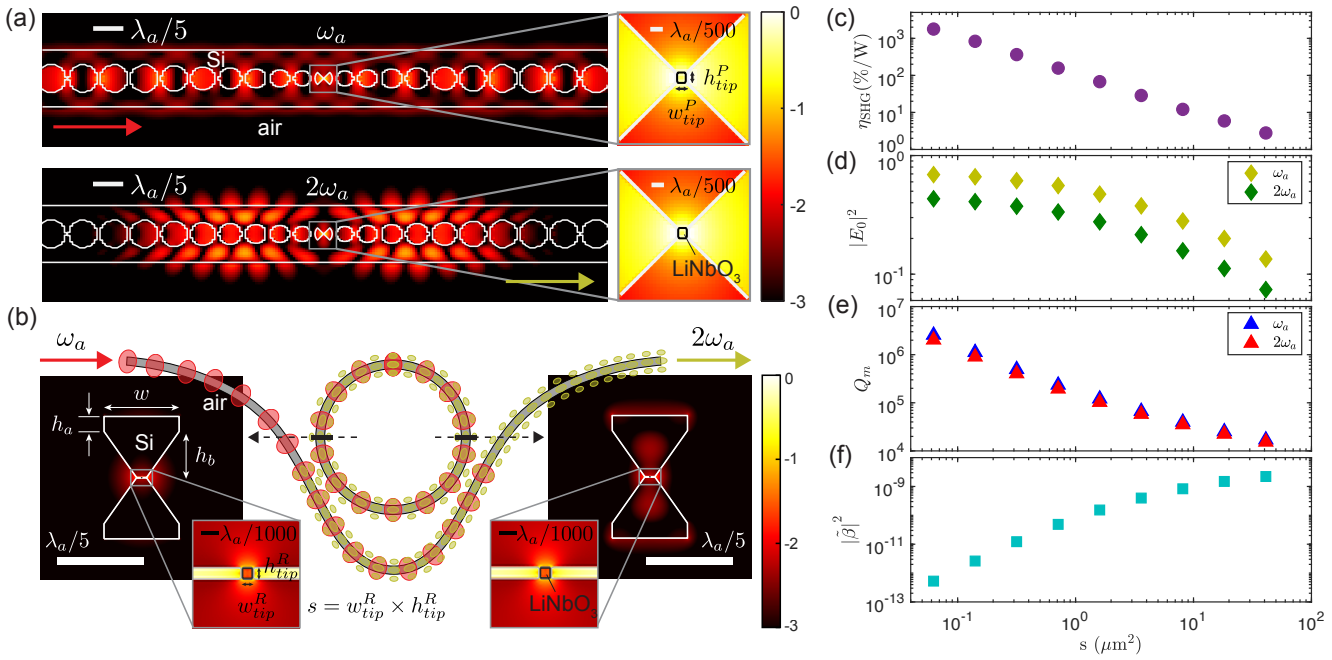

FIG. 3. Cavity modes and scaling behavior. (a) Top-view of the field profiles ($\log_{10}\left|\frac{\mathbf{E}}{\mathbf{E}_{max}}\right|^2$) of PhC cavity modes (TE) at $\omega_a = 331$ GHz (top) and $\omega_b = 662$ GHz (bottom). The thickness of the cavity (out of plane) is $\sim 0.153\lambda_a$. Scale-bars are $\lambda_a/5$ ($\lambda_a/500$ for close-ups). Note that we only show 10 holes on each side for the visibility while the whole structure has 32 holes on each side. (b) Side-view of the field profiles in the ring for TM (vertically polarized) modes at $\omega_a = 350$ GHz (left), $\omega_b = 700$ GHz (right). Here, $LiNbO_3$ is used as the nonlinear material and Si as the host material for both the PhC and ring cavities. (c) The SHG efficiencies with cross-sectional area s of nonlinear material in the ring resonator, for conversion from 350 GHz to 700 GHz. (d) Normalized electric field square in the tip $|E_0|^2 = \left(\frac{\lambda_a}{n_a}\right)^3 \frac{\epsilon_{\text{tip}}|\mathbf{E}_{\text{tip}}|^2}{\int \epsilon(\mathbf{r})|\mathbf{E}(\mathbf{r})|^2 d^3\mathbf{r}}$ where $|\mathbf{E}_{\text{tip}}|$ is the average field amplitude in the nonlinear material. (e) Material quality factor. (f) Magnitude squared of normalized nonlinear overlap $|\tilde{\beta}|^2$, calculated for a ring radius of $3.6\lambda_a$.

III. CAVITY DESIGNS

Dielectric cavities with strong field confinement and high quality factors were recently studied [8, 9, 42, 43] and experimentally demonstrated [44]. These designs introduce tip structures at the anti-node of a mode resulting in extreme field enhancement at the dielectric tip.

Here, we apply this field concentration principle to the THz regime to design hybrid-material PhC and ring cavities with large SHG conversion efficiency. Both cavity types have unique benefits and challenges; PhC cavities have smaller mode volume and do not need phase matching; ring cavities require phase matching but the radiation Q is less sensitive to imperfections and easier to couple to a waveguide without modification.

Fig. 3(a) shows the FD (top) and SH mode (bottom) of our nanobeam PhC cavity design (at the middle cross-section). The holes in the rectangular waveguide form a Bragg reflector. The tapering of the hole radii creates defect modes in the bandgap. The dielectric field concentration tips are introduced in the center hole [42]. A rectangular nanowire made of nonlinear medium sits between the two concentric tips where the electric field is strongest (inset). One can position nanowires using a transfer setup [45].

Fig. 3(b) shows a top view of our ring cavity (middle) and cross sectional profiles of the FD (left) and SH mode (right). Interferometric coupling [46] can be used for tuning of the coupling Q factor, $Q^c_{a(b)}$, that optimizes the conversion efficiency (see Appendix A).This type of cavity can be fabricated by combining two separately fabricated ring resonators with angled cross sections, one with a thin nonlinear medium on top of the silicon.

We use the $\chi^{(2)}_{33}$ component to couple the fundamental transverse magnetic (TM) mode at ω_a and a higher order TM mode at $2\omega_a$. To couple the two TM modes by the $\chi^{(2)}_{14}$ component in the zinc-blende materials, the dominant electric field component should be aligned to the [111] crystal axis [47], in which case $\chi^{(2)}_{\text{eff}} = \frac{2}{\sqrt{3}}\chi^{(2)}_{14}$. The ring design achieves phase matching by the condition on the angular wavenumber, $m_b - 2m_a = 0$. Selecting the radius such that the ring is resonant at the frequencies ω_a and $2\omega_a$, for which the effective indices of the waveguide are equal, fulfills the energy matching condition. Appendix C provides more details on the cavity designs.

Figs. 3(c-f) illustrate how our hybrid cavity designs enable large SHG conversion efficiencies using the ring cav-

ity as an example. Here we assume the cavity host material (Si) to be lossless, which is a good approximation considering high-resistivity Si has material quality factors of $\gtrsim 10^6$ (see Appendix C for a discussion of losses in Si). The insets in Fig. 3(a) and (b) show that the nonlinear material is embedded only near the tip where both cavity modes have a high electric energy density [48]. The material quality factor $Q^m_{a(b)}$ is proportional to the inverse of the fraction of energy in the $\chi^{(2)}$ material (see Appendix C).

As shown in Fig. 3(c), which plots the conversion efficiency η_{SHG} as a function of the cross-sectional area s of the nonlinear medium, the efficiency increases as the size of the nonlinear medium is reduced. Fig. 3(d) plots the normalized electric field square $|E_0|^2$ in the nonlinear material. As $|E_0|^2$ increases with decreasing nonlinear material volume, $Q^m_{a(b)}$ also increases, as plotted in Fig. 3(e). The nonlinear mode overlap $|\tilde{\beta}|$ decreases with nonlinear material volume (see Fig. 3(f)), but η_{SHG} increases since it is proportional to the quality factor cubed. This increase saturates when the total quality factor is dominated by radiation loss.

IV. CONVERSION EFFICIENCIES

Fig. 4 plots the THz SHG conversion efficiencies in the nondepleted pump regime for different nonlinear materials. For the PhC design, we also show projected efficiencies for improved radiation quality factor $Q^r_{a(b)}$. We designed PhC cavities with a nonlinear material volume small enough for $Q_{a(b)}$ to be limited by radiation loss, and ring cavities with $Q_{a(b)}$ limited largely by material loss. For simplicity, we ignore the index dispersion, considering instead the dispersion of loss and nonlinear coefficients.

The conversion efficiencies are above 10^3%/W for the current designs across most of the THz gap, indicating near-unity conversion efficiencies with input powers on the order of hundreds of milliwatts. Analysis of the absolute conversion efficiency (depleted pump regime) provides the output power at each stage of the cascaded process, shown in Fig. 1(a) for the ring (see further discussion in Appendix A).

V. DISCUSSION

We theoretically estimated the first- and second-order susceptibility of several promising materials in the terahertz region: GaAs, GaP, ZnTe, $LiNbO_3$, and $LiTaO_3$. Quantum materials such as charge density wave materials (TaS_2), excitonic insulators (Ta_2NiS_5), and collective excitations in superconductors such as niobium nitride may enable even higher second harmonic efficiency or signal amplification, though we leave a detailed analysis with proper accounting of loss for future work. As the ultimate limit to field concentration into a nonlinear material, future work should also consider THz-band nonlinearities in graphene [49].

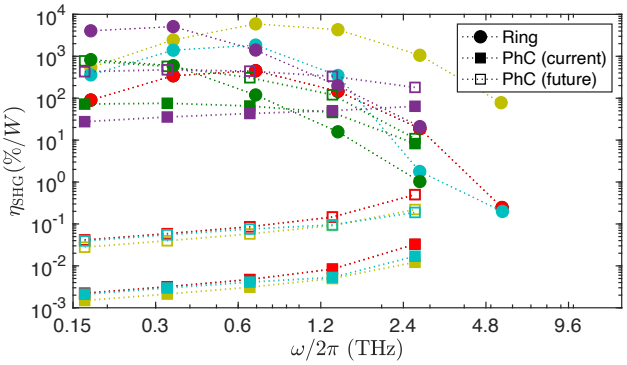

FIG. 4. Maximum second harmonic generation efficiency for doubling frequencies, in %/W. Colors denote the materials as in Fig. 2. Solid and hollow markers represent the current design and near-future designs with improved Q, respectively. For the photonic crystal cavities, $Q^{\mathrm{r}}_a = 358,000$ (10^6) and $Q^{\mathrm{r}}_b = 41,600$ (10^5) for the current (near-future) designs. The cross-sectional area of the nonlinear material is 1 μm × 1μm for 331 GHz, and inversely proportional to the square of frequencies. For the ring cavities, we calculate $Q^{\mathrm{r}}_{a,b} \geq 10^6$, and the cross-sectional area of the nonlinear material is fixed to 100 nm × 100 nm at every frequency. For all calculations, the silicon is assumed to be lossless. Note that the efficiencies at 2.6 THz for ZnTe and at 5.2 THz for GaAs, ZnTe, $LiTaO_3$, and $LiNbO_3$ can deviate from the estimation due to Miller's rule's inaccuracy.

A key to minimizing optical loss is to embed such materials in regions of high field concentration: hybrid dielectric cavities employing dielectric tip structures in photonic crystal cavities and ring resonators. We anticipate that substantial efficiency gains will be possible by co-design of materials, resonators, and SHG phase matching. These efforts also call for experimental studies of THz-spectrum nonlinearities, cavities, loss mechanisms, etc. These dielectric field concentration structures are also promising as low-loss alternatives to doubly resonant metallic nanoantennas, which underpin an exciting recent proposal for THz-to-optical parametric frequency conversion at the single photon level [50].

From the calculations of non-depleted and absolute conversion efficiencies of our devices over a sequence of cascaded frequency doubling steps, we estimate the opportunity to fill the THz gap with 1 W of input power, generating THz radiation with substantially higher efficiency than electronic sources alone, but without the need for cryogenic cooling in THz lasers. It is clear from the curves in Fig. 1 that the fall-off in output power is very sudden, since cascaded losses compound in each SHG step. To sustain high output power after many SHG steps, we therefore considered a rather high input power of up to 4 W at the ∼100 GHz seed frequency. Due to limitations imposed by dielectric breakdown, high input powers may require larger cavities in the early stages of

frequency conversion to distribute gain, or coherent combination of multiple cavity outputs between stages to operate below damage threshold while compensating losses in each step. The back reflection of the cavities can reduce the efficiencies of the devices, but the isolation can quadratically suppress it. Moreover, one can make use of to boost efficiencies up to $\approx \times 1.618$ given one can precisely control the back reflection. If the phase coming from reflection and the propagation between stages is random and not controllable, isolation can quadratically suppress the back reflection, and high isolation guarantees minimum efficiency only reduced by the reflectance. (See Appendix D and Appendix E for an analysis of dielectric breakdown and back reflection, respectively.)

VI. CONCLUSION

We proposed an approach for light sources in the THz spectrum based on cascaded second harmonic generation pumped by low-noise electronic oscillators. As opposed to laser sources, this approach requires no population inversion; and in contrast to electronic sources, where ohmic loss limits high-frequency operation, our dominant loss originates from dielectric absorption and radiation. It leverages high quality factor dielectric resonators with phonon-resonance-enhanced second-order nonlinearity for parametric frequency conversion, which is inherently power-preserving. In particular, our modeling shows that the proposed devices provide sufficiently high SHG conversion efficiency to be cascaded over multiple octaves, provided sufficiently high input power from the electronic source. Moreover, sum/difference frequency generation (SFG/DFG) would enable arbitrary frequencies. Using a combination of cascaded SHG, SFG, and DFG, our approach opens the door to compact, low-cost, and room temperature devices that deliver high power THz radiation at any frequencies in the THz gap, and that may be extended into the mid-IR and beyond. Though we focused our discussion in electronic nonlinearities, the method can be trivially extended to magnetic light-matter interaction [51]. Moreover, an efficient nonlinear cavity devices can be used for quantum applications such as a THz single photon source with spontaneous parametric down-conversion (SPDC) and cluster state generation with optical parametric oscillators (OPO) [52] for a large-scale fault-tolerant quantum computing [53].

ACKNOWLEDGMENTS

The authors thank C. Panuski and M. El Kabbash for helpful feedback. This work was supported in part by the Defense Advanced Research Projects Agency (DARPA) DRINQS (HR001118S0024) program and the MITRE Quantum Moonshot program. L.A. was supported by the National Science Foundation Graduate Research Fellowship (Grant No. 1745302). H.C. was supported in part by the Claude E. Shannon Research Assistantship and Samsung Scholarship.

DISCLOSURES

The authors declare no conflicts of interest.

CONTRIBUTIONS

D.E. and H.C. conceived and initiated the presented idea. L.A. analyzed nonlinear susceptibilities. H.C. proposed anisotropic anharmonicity for nonlinearity correction. H.C. designed the doubly resonant PhC cavity. L.A. designed the ring cavity. M.H. simulated equation of motion in non-depletion regime. All authors contributed in writing manuscript.

[1] R. A. Lewis, A review of terahertz sources, J. Phys. D: Appl. Phys. **47**, 374001 (2014).
[2] R. Han, Z. Hu, C. Wang, J. Holloway, X. Yi, M. Kim, and J. Mawdsley, Filling the gap: Silicon terahertz integrated circuits offer our best bet, IEEE Microw. Mag. **20**, 80 (2019).
[3] K. Sengupta, T. Nagatsuma, and D. M. Mittleman, Terahertz integrated electronic and hybrid electronic–photonic systems, Nat. Electron. **1**, 622 (2018).
[4] H. Aghasi, S. Naghavi, M. Tavakoli Taba, M. Aseeri, A. Cathelin, and E. Afshari, Terahertz electronics: Application of wave propagation and nonlinear processes, Appl. Phys. Rev. **7**, 021302 (2020).
[5] E. B. Petersen, W. Shi, A. Chavez-Pirson, N. Peyghambarian, and A. T. Cooney, Efficient parametric terahertz generation in quasi-phase-matched gap through cavity enhanced difference-frequency generation, Appl. Phys. Lett. **98**, 121119 (2011).
[6] K. Fujita, S. Jung, Y. Jiang, J. H. Kim, A. Nakanishi, A. Ito, M. Hitaka, T. Edamura, and M. A. Belkin, Recent progress in terahertz difference-frequency quantum cascade laser sources, Nanophotonics **7**, 1795 (2018).
[7] S. Perkowitz, Navigating the terahertz gap, Phys. World **33**, 37 (2020).
[8] H. Choi, M. Heuck, and D. Englund, Self-similar nanocavity design with ultrasmall mode volume for single-photon nonlinearities, Phys. Rev. Lett. **118**, 223605 (2017).
[9] S. Hu and S. M. Weiss, Design of photonic crystal cavities for extreme light concentration, ACS photonics **3**, 1647 (2016).

[10] M. Tonouchi, Cutting-edge terahertz technology, Nat. Photon. **1**, 97 (2007).

[11] T. A. Midford and R. L. Bernick, Millimeter-wave cw impatt diodes and oscillators, IEEE Trans. Microw. Theory Techn. **27**, 483 (1979).

[12] W. C. Niehaus, T. E. Seidel, and D. E. Iglesias, Double-drift impatt diodes near 100 ghz, IEEE Trans. Electron Devices **20**, 765 (1973).

[13] M. Urteaga, Z. Griffith, M. Seo, J. Hacker, and M. J. Rodwell, InP HBT technologies for THz integrated circuits, Proc. IEEE **105**, 1051 (2017).

[14] K. M. Leong, X. Mei, W. Yoshida, P.-H. Liu, Z. Zhou, M. Lange, L.-S. Lee, J. G. Padilla, A. Zamora, B. S. Gorospe, *et al.*, A 0.85 THz low noise amplifier using InP HEMT transistors, IEEE Microw. Wirel. Compon. Lett. **25**, 397 (2015).

[15] R. Izumi, T. Sato, S. Suzuki, and M. Asada, Resonant-tunneling-diode terahertz oscillator with a cylindrical cavity for high-frequency oscillation, AIP Adv. **9**, 085020 (2019).

[16] Y. Jin, J. L. Reno, and S. Kumar, Phase-locked terahertz plasmonic laser array with 2 W output power in a single spectral mode, Optica **7**, 708 (2020).

[17] J. Luo, T. Jiang, C. Shen, X. Wang, Z. Zhan, J. Yu, R. Zou, J. Li, Y. Zeng, and W. Wu, Distributed feedback 2.5-terahertz quantum cascade laser with high-power and single-mode emission, Opt. Eng. **59**, 026109 (2020).

[18] L. Li, L. Chen, J. Freeman, M. Salih, P. Dean, A. Davies, and E. Linfield, Multi-watt high-power THz frequency quantum cascade lasers, Electron. Lett. **53**, 799 (2017).

[19] T. A. Bondaz, A. Laurain, J. V. Moloney, and J. G. McInerney, Generation and stabilization of continuous-wave THz emission from a bi-color VECSEL, IEEE Photonics Technol. Lett. **31**, 1569 (2019).

[20] D. Yan, Y. Wang, D. Xu, P. Liu, C. Yan, J. Shi, H. Liu, Y. He, L. Tang, J. Feng, *et al.*, High-average-power, high-repetition-rate tunable terahertz difference frequency generation with gase crystal pumped by 2 μm dual-wavelength intracavity ktp optical parametric oscillator, Photonics Res. **5**, 82 (2017).

[21] R. W. Boyd, *Nonlinear optics* (Elsevier, 2003).

[22] W. Faust, C. Henry, and R. Eick, Dispersion in the nonlinear susceptibility of GaP near the reststrahl band, Phys. Rev. **173**, 781 (1968).

[23] C. Flytzanis and J. Ducuing, Second-order optical susceptibilities of III-V semiconductors, Phys. Rev. **178**, 1218 (1969).

[24] C. Garrett, Nonlinear optics, anharmonic oscillators, and pyroelectricity, IEEE J. Quantum Electron. **4**, 70 (1968).

[25] T. Dekorsy, V. A. Yakovlev, W. Seidel, M. Helm, and F. Keilmann, Infrared-phonon-polariton resonance of the nonlinear susceptibility in GaAs, Phys. Rev. Lett. **90**, 055508 (2003).

[26] A. Mayer and F. Keilmann, Far-infrared nonlinear optics. I. $\chi^{(2)}$ near ionic resonance, Phys. Rev. B **33**, 6954 (1986).

[27] W. Faust and C. H. Henry, Mixing of visible and near-resonance infrared light in GaP, Phys. Rev. Lett. **17**, 1265 (1966).

[28] A. S. Barker Jr, Dielectric dispersion and phonon line shape in gallium phosphide, Phys. Rev. **165**, 917 (1968).

[29] B. Carnio and A. Elezzabi, An extensive finite-difference time-domain formalism for second-order nonlinearities based on the Faust-Henry dispersion model: Application to terahertz generation, J. Infrared Millim. Terahertz Waves , 1 (2020).

[30] T. Hattori, Y. Homma, A. Mitsuishi, and M. Tacke, Indices of refraction of ZnS, ZnSe, ZnTe, CdS, and CdTe in the far infrared, Opt. Commun. **7**, 229 (1973).

[31] A. S. Barker, A. A. Ballman, and J. A. Ditzenberger, Infrared study of the lattice vibrations in $LiTaO_3$, Phys. Rev. B **2**, 4233 (1970).

[32] A. S. Barker and R. Loudon, Dielectric properties and optical phonons in $LiNbO_3$, Phys. Rev. **158**, 433 (1967).

[33] S. Kojima, H. Kitahara, S. Nishizawa, and M. W. Takeda, Dielectric properties of ferroelectric lithium tantalate crystals studied by terahertz time-domain spectroscopy, Jpn. J. Appl. Phys. **42**, 6238 (2003).

[34] S. Kojima and T. Mori, Broadband terahertz time-domain spectroscopy of ferroelectric $LiTaO_3$: Phonon-polariton dispersion, in *AIP Conference Proceedings*, Vol. 1627 (American Institute of Physics, 2014) pp. 52–57.

[35] D. Grischkowsky, S. Keiding, M. Van Exter, and C. Fattinger, Far-infrared time-domain spectroscopy with terahertz beams of dielectrics and semiconductors, J. Opt. Soc. Am. B **7**, 2006 (1990).

[36] G. Boyd, T. Bridges, M. Pollack, and E. Turner, Microwave nonlinear susceptibilities due to electronic and ionic anharmonicities in acentric crystals, Phys. Rev. Lett. **26**, 387 (1971).

[37] B. Levine, Bond-charge calculation of nonlinear optical susceptibilities for various crystal structures, Phys. Rev. B **7**, 2600 (1973).

[38] Z. H. Levine and D. C. Allan, Calculation of the nonlinear susceptibility for optical second-harmonic generation in iii-v semiconductors, Phys. Rev. Lett. **66**, 41 (1991).

[39] F. Wang, Calculation of the electro-optical and nonlinear optical coefficients of ferroelectric materials from their linear properties, Phys. Rev. B **59**, 9733 (1999).

[40] J. Zhang, K. Yao, Z. Liu, G. Gao, Z. Sun, and S. Fan, First-principles study of the ferroelectric and nonlinear optical properties of the linbo 3-type znsno 3, Phys. Chem. Chem. Phys. **12**, 9197 (2010).

[41] A. Ratnaparkhe and W. R. Lambrecht, Calculated phonon modes, infrared, and raman spectra in zngega2n4, J. Appl. Phys. **128**, 075702 (2020).

[42] H. Choi, D. Zhu, Y. Yoon, and D. Englund, Cascaded cavities boost the indistinguishability of imperfect quantum emitters, Phys. Rev. Lett. **122**, 183602 (2019).

[43] Q. Lu, X. Chen, H. Yang, X. Wu, and S. Xie, Ultrahigh purcell factor, improved sensitivity, and enhanced optical force in dielectric bowtie whispering-gallery-mode resonators, IEEE Photon. J. **9**, 1 (2017).

[44] Z. Hu, M. Kaynak, and R. Han, High-power radiation at 1 THz in silicon: A fully scalable array using a multi-functional radiating mesh structure, IEEE J. Solid-State Circuits **53**, 1313 (2018).

[45] M. Notomi, M. Takiguchi, S. Sergent, G. Zhang, and H. Sumikura, Nanowire photonics toward wide wavelength range and subwavelength confinement, Opt. Mater. Express **10**, 2560 (2020).

[46] C. K. Madsen, G. Lenz, A. J. Bruce, M. A. Cappuzzo, L. T. Gomez, and R. E. Scotti, Integrated all-pass filters for tunable dispersion and dispersion slope compensation, IEEE Photon. Technol. Lett. **11**, 1623 (1999).

[47] S. Buckley, M. Radulaski, K. Biermann, and J. Vučković, Second harmonic generation in photonic crystal cavities

in (111)-oriented GaAs, Appl. Phys. Lett. **103**, 211117 (2013).
[48] S. Mouradian, T. Schröder, J. Zheng, T.-J. Lu, H. Choi, N. Wan, M. Walsh, E. Bersin, and D. Englund, Nv-based quantum memories coupled to photonic integrated circuits, in *Active Photonic Materials VIII*, Vol. 9920 (SPIE, 2016) pp. 69–74.
[49] H. A. Hafez, S. Kovalev, K.-J. Tielrooij, M. Bonn, M. Gensch, and D. Turchinovich, Terahertz nonlinear optics of graphene: From saturable absorption to high-harmonics generation, Adv. Opt. Mater. **8**, 1900771 (2020).
[50] P. Roelli, D. Martin-Cano, T. J. Kippenberg, and C. Galland, Molecular platform for frequency upconversion at the single-photon level, Phys. Rev. X **10**, 031057 (2020).
[51] H. Choi and D. Englund, Ultrastrong magnetic light-matter interaction with cavity mode engineering, arXiv preprint arXiv:2108.13266 (2021).
[52] N. C. Menicucci, S. T. Flammia, and O. Pfister, One-way quantum computing in the optical frequency comb, Phys. Rev. Lett. **101**, 130501 (2008).
[53] H. Choi, M. Pant, S. Guha, and D. Englund, Percolation-based architecture for cluster state creation using photon-mediated entanglement between atomic memories, Npj Quantum Inf. **5**, 1 (2019).
[54] X. Guo, C.-L. Zou, and H. X. Tang, Second-harmonic generation in aluminum nitride microrings with 2500%/W conversion efficiency, Optica **3**, 1126 (2016).
[55] J. D. Joannopoulos, S. G. Johnson, J. N. Winn, and R. D. Meade, Molding the flow of light, Princeton Univ. Press, Princeton, NJ (2008).
[56] Z. Lin, X. Liang, M. Lončar, S. G. Johnson, and A. W. Rodriguez, Cavity-enhanced second-harmonic generation via nonlinear-overlap optimization, Optica **3**, 233 (2016).
[57] Z. Vernon, M. Liscidini, and J. Sipe, Quantum frequency conversion and strong coupling of photonic modes using four-wave mixing in integrated microresonators, Phys. Rev. A **94**, 023810 (2016).
[58] C. M. Reinke, A. Jafarpour, B. Momeni, M. Soltani, S. Khorasani, A. Adibi, Y. Xu, and R. K. Lee, Nonlinear finite-difference time-domain method for the simulation of anisotropic,/spl chi//sup (2)/, and/spl chi//sup (3)/optical effects, J. Light. Technol. **24**, 624 (2006).
[59] M. Moradi, S.-M. Pourangha, V. Nayyeri, M. Soleimani, and O. M. Ramahi, Unconditionally stable fdtd algorithm for 3-d electromagnetic simulation of nonlinear media, Opt. Express **27**, 15018 (2019).
[60] A. Paarmann, I. Razdolski, A. Melnikov, S. Gewinner, W. Schöllkopf, and M. Wolf, Second harmonic generation spectroscopy in the reststrahl band of sic using an infrared free-electron laser, Appl. Phys. Lett. **107**, 081101 (2015).
[61] M. Barmentlo, E. Eliel, E. van der Ham, Q. Vrehen, A. van der Meer, P. van Amersfoort, *et al.*, Sum-frequency generation with a free-electron laser: A study of gallium phosphide, Phys. Rev. A **50**, R14 (1994).
[62] W.-T. Liu and Y. Shen, Sum-frequency phonon spectroscopy on α-quartz, Phys. Rev. B **78**, 024302 (2008).
[63] R. C. Miller, Optical second harmonic generation in piezoelectric crystals, Appl. Phys. Lett. **5**, 17 (1964).
[64] J. Dai, J. Zhang, W. Zhang, and D. Grischkowsky, Terahertz time-domain spectroscopy characterization of the far-infrared absorption and index of refraction of high-resistivity, float-zone silicon, J. Opt. Soc. Am. B **21**, 1379 (2004).
[65] J. Krupka, P. Kamiński, and L. Jensen, High q-factor millimeter-wave silicon resonators, IEEE Trans. Microw. Theory Techn. **64**, 4149 (2016).
[66] M. Van Exter and D. Grischkowsky, Carrier dynamics of electrons and holes in moderately doped silicon, Phys. Rev. B **41**, 12140 (1990).
[67] L. Berger, Dielectric strength of insulating materials, Carbon **1**, 2 (2006).
[68] M. S. Shur, *Handbook series on semiconductor parameters*, Vol. 1 (World Scientific, 1996).
[69] H. Hirori, A. Doi, F. Blanchard, and K. Tanaka, Single-cycle terahertz pulses with amplitudes exceeding 1 mv/cm generated by optical rectification in linbo 3, Appl. Phys. Lett. **98**, 091106 (2011).
[70] Y. Sun, S. Boggs, and R. Ramprasad, The intrinsic electrical breakdown strength of insulators from first principles, Appl. Phys. Lett. **101**, 132906 (2012).
[71] V. Dmitriev, S. L. M. da Silva, and W. Castro, Ultra-wideband graphene three-port circulator for thz region, Opt. Express **27**, 15982 (2019).
[72] A. Grebenchukov, V. Ivanova, A. Suslov, G. Kropotov, and M. Khodzitskiy, Broadband terahertz isolator, IEEE Trans. Terahertz Sci. Technol. (2021).
[73] S. Yuan, L. Chen, Z. Wang, W. Deng, Z. Hou, C. Zhang, Y. Yu, X. Wu, and X. Zhang, On-chip terahertz isolator with ultrahigh isolation ratios, Nat. Commun. **12**, 1 (2021)

Appendix A: Conversion Efficiency

The conversion efficiency of second-harmonic generation (SHG) can be derived from the Hamiltonian describing a doubly-resonant cavity coupled to waveguide modes at both fundamental and second-harmonic (SH) frequency [54]

$$\mathcal{H}/\hbar = \delta_a \hat{a}^\dagger \hat{a} + \delta_b \hat{b}^\dagger \hat{b} + \left[g(\hat{a}^\dagger)^2 \hat{b} + g^* \hat{a}^2 \hat{b}^\dagger \right] + \sqrt{2\kappa_a^c}(\hat{\epsilon}_p^\dagger \hat{a} + \hat{\epsilon}_p \hat{a}^\dagger) + \sqrt{2\kappa_b^c}(\hat{\epsilon}_{\mathrm{SHG}}^\dagger \hat{b} + \hat{\epsilon}_{\mathrm{SHG}} \hat{b}^\dagger). \tag{A1}$$

The operators $\hat{a}$ and $\hat{b}$ annihilate a photon from the FD and SH mode of the cavity, while $\hat{\epsilon}_p$ ($\hat{\epsilon}_{\mathrm{SHG}}$) is the annihilation operator for input (output) photons in the waveguide. We used quantum field operators generality (to include potential quantum applications such as SPDC or OPO (see VI. Conclusion)), but operators can be replaced with c-numbers for SHG, as we will see soon. The resonance frequencies of the cavity modes are ω_a and $\omega_b = 2\omega_a$ while the carrier frequency of the input (output) field is ω_p ($2\omega_p$). Note that Eq. (A1) is expressed in a frame rotating with ω_p and $2\omega_p$ for $\hat{a}$ and $\hat{b}$, which introduces the detunings $\delta_a = \omega_a - \omega_p$ and $\delta_b = \omega_b - 2\omega_p$. The cavity-waveguide coupling

rate of the fundamental (SH) mode is κ_a^c (κ_b^c) and the nonlinear coupling rate g can be derived from perturbation theory [8, 55]

$$g = \chi^{(2)}_{\text{eff}} \sqrt{\frac{\hbar\omega_a^2\omega_b}{\epsilon_0}} \frac{\tilde{\beta}}{\sqrt{(\lambda_a/n_a)^3}}, \tag{A2}$$

where the normalized field overlap factor, $\tilde{\beta}$, is given by

$$\tilde{\beta} = \frac{1}{\chi^{(2)}_{\text{eff}}} \frac{\int dV \chi^{(2)}_{ijk}(\vec{r}) E_{a,i}(\vec{r}) E_{a,j}(\vec{r}) E^*_{b,k}(\vec{r})}{\int dV \epsilon(\vec{r}) \left|\vec{E}_a(\vec{r})\right|^2 \sqrt{\int dV \epsilon(\vec{r}) \left|\vec{E}_b(\vec{r})\right|^2}} \sqrt{\frac{\lambda_a^3}{n_a^3}}. \tag{A3}$$

Note that $\tilde{\beta}$ is normalized to the wavelength in the nonlinear medium in contrast to $\bar{\beta}$ in [56], which is normalized to the vacuum wavelength. The normalization is chosen for fair comparison between nonlinear materials. We used Einstein notation implying summation over the repeated Cartesian subscripts $(i, j, k) \in (x, y, z)$. The field profiles of the unperturbed cavity modes are $\vec{E}_a(\vec{r})$ and $\vec{E}_b(\vec{r})$ and n_a is the refractive index at ω_a. The equations of motion of the cavity modes $\hat{a}$ and $\hat{b}$ can be derived from the Heisenberg equation of motion $i\hbar\frac{d\hat{O}}{dt} = \left[\hat{O}, \mathcal{H}\right]$ where $\hat{O}$ is the cavity mode operators

$$\frac{d\hat{a}}{dt} = [-i\delta_a - \kappa_a^c]\hat{a} - i2g\hat{a}^\dagger\hat{b} + i\sqrt{2\kappa_a^c}\hat{\epsilon}_p, \tag{A4a}$$

$$\frac{d\hat{b}}{dt} = [-i\delta_b - \kappa_b^c]\hat{b} - ig^*\hat{a}^2. \tag{A4b}$$

Note that Eq. (A4) assumes that there is no incident field at ω_b. Assuming that all fields are in strong coherent states, we make the replacement of operators with c-numbers [57] $\hat{a} \to \alpha_a$, $\hat{b} \to \alpha_b$, $\hat{\epsilon}_p \to \epsilon_p$, $\hat{\epsilon}_{\text{SHG}} \to \epsilon_{\text{SHG}}$. This results in equations of motion and input-output relations for the c-numbers that are normalized such that the square of their absolute values correspond to the number of photons in the cavity modes and photon flux in the waveguide

$$\frac{d\alpha_a}{dt} = [-i\delta_a - \kappa_a]\alpha_a - i2g\alpha_a^*\alpha_b + i\sqrt{2\kappa_a^c}\epsilon_p, \tag{A5a}$$

$$\frac{d\alpha_b}{dt} = [-i\delta_b - \kappa_b]\alpha_b - ig^*\alpha_a^2, \tag{A5b}$$

$$\epsilon_p^{\text{out}} = \epsilon_p - \sqrt{2\kappa_a^c}\alpha_a, \tag{A5c}$$

$$\epsilon_{\text{SHG}} = -\sqrt{2\kappa_b^c}\alpha_b. \tag{A5d}$$

In Eq. (A5), we introduced the total decay rates, $\kappa_{a(b)} = \kappa^c_{a(b)} + \kappa^m_{a(b)} + \kappa^r_{a(b)}$, where the superscripts correspond to waveguide-coupling (c), material absorption (m), and radiation loss (r). We consider a continuous wave (CW) input and steady-state, where $d\alpha_{a(b)}/dt = 0$. In the limit of low conversion efficiency, we use the non-depleted pump approximation, which neglects the nonlinear term in Eq. (A5a). In this case, we have

$$\alpha_a = \frac{i\sqrt{2\kappa_a^c}\epsilon_p}{-i\delta_a - \kappa_a}, \quad \text{and} \quad \alpha_b = \frac{ig^*}{-i\delta_b - \kappa_b}\alpha_a^2. \tag{A6}$$

The optical power in the input and output waveguides are $P_p = \hbar\omega_a|\epsilon_p|^2$ and $P_{\text{SHG}} = \hbar\omega_b|\epsilon_{\text{SHG}}|^2$, respectively. From Eqs. (A6) and (A5d), we have

$$P_{\text{SHG}} = \hbar\omega_b\left|\sqrt{2\kappa_b^c}\alpha_b\right|^2 = \hbar\omega_b 2|g|^2\frac{\kappa_b^c}{\delta_b^2+\kappa_b^2}|\alpha_a|^4 = \frac{\hbar\omega_b 2|g|^2\kappa_b^c}{\delta_b^2+\kappa_b^2}\frac{4(\kappa_a^c)^2}{\left(\delta_a^2+\kappa_a^2\right)^2}|\epsilon|^4 = \frac{\hbar\omega_b 2|g|^2\kappa_b^c}{\delta_b^2+\kappa_b^2}\frac{4(\kappa_a^c)^2}{\left(\delta_a^2+\kappa_a^2\right)^2}\frac{P_p^2}{\hbar^2\omega_a^2}. \tag{A7}$$

The output power is maximized when $\delta_a = \delta_b = 0$, in which case Eq. (A7) becomes

$$P_{\text{SHG}} = \frac{16}{\hbar\omega_a}|g|^2\frac{2Q_b}{\omega_b}\frac{4Q_a^2}{\omega_a^2}\left(\frac{\kappa_a^c}{\kappa_a}\right)^2\frac{\kappa_b^c}{\kappa_b}P_p^2 = \frac{64}{\hbar\omega_a^4}|g|^2Q_a^2Q_b\left(\frac{Q_a}{Q_a^c}\right)^2\frac{Q_b}{Q_b^c}P_p^2, \tag{A8}$$

where we used $Q_{a(b)} = \omega_{a(b)}/(2\kappa_{a(b)})$. The non-depleted conversion efficiency is therefore given by

$$\eta_{\text{SHG}} \equiv \frac{P_{\text{SHG}}}{P_p^2} = \frac{64}{\hbar\omega_a^4}|g|^2Q_a^2Q_b\eta_c, \tag{A9}$$

where the input-output coupling efficiency is defined as

$$\eta_c \equiv \left(\frac{Q_a}{Q_a^c}\right)^2 \frac{Q_b}{Q_b^c}. \tag{A10}$$

From Eq. (A7) we find that the non-depleted conversion efficiency is maximized when $\kappa^c_{a(b)} = \kappa^m_{a(b)} + \kappa^r_{a(b)}$ corresponding to critical coupling.

In the limit of large conversion efficiency, we solve Eq. (A5) to evaluate the absolute conversion efficiency, $\eta^{\rm abs}_{\rm SHG} \equiv P_{\rm SHG}/P_p$, where $P_{\rm SHG}$ is calculated without making the non-depleted pump approximation. In this case, the optimum coupling Q must be determined via numerical optimization. In Fig. 5(a) we show an example of the absolute conversion efficiency as a function of input power and the corresponding values of $Q^c_{a(b)}$ are plotted in Fig. 5(b).

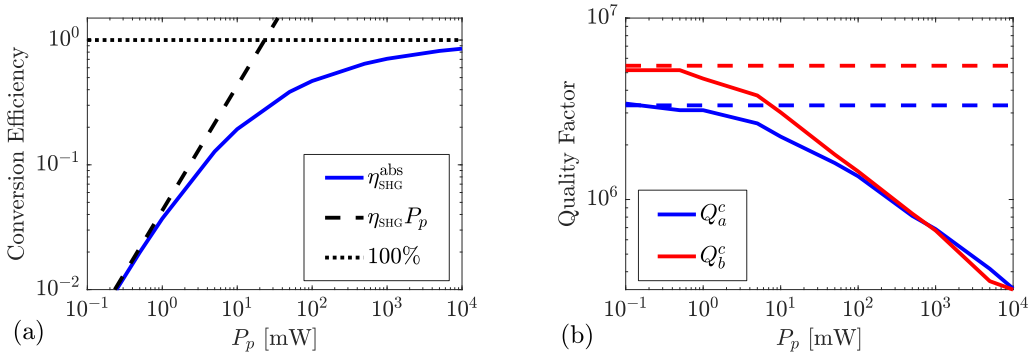

FIG. 5. Example of a calculation of the absolute conversion efficiency for the ring cavity design. (a) $\eta^{\rm abs}_{\rm SHG}$ is plotted as a function of input power. The black dashed line plots $\eta_{\rm SHG} P_p$ from Eq. (A9), which asymptotically approaches $\eta^{\rm abs}_{\rm SHG}$ at low input power. (b) Optimum choice of coupling quality factors corresponding to $\eta^{\rm abs}_{\rm SHG}$ in (a). $Q^c_{a(b)}$ approach their values at critical coupling (dashed lines) at low power levels as expected. The parameters used in Eq. (A5) to calculate $\eta^{\rm abs}_{\rm SHG}$ correspond to a ring cavity design using GaP as the nonlinear material at a frequency of $\omega_a/2\pi = 1385\,$GHz. The parameter values are: $Q^r_a = 6.0\times10^6$, $Q^r_b = 2.0\times10^{13}$,$Q^m_a = 7.3\times10^6$, $Q^m_b = 5.5\times10^6$, $|\tilde{\beta}| = 2.4\times10^{-5}$, $n_a = 3.32$, and $\chi^{(2)}_{\rm eff} = 1.2\times10^{-10}$m/V.

To calculate the power at each frequency of the cascaded SHG plotted in Fig. 1 of the main text, we first calculate $\eta^{\rm abs}_{\rm SHG}$ as a function of input power at each frequency for the different materials illustrated in Fig. 4. At each frequency, the material resulting in the largest conversion efficiency is chosen and the output power at ω_b becomes the input power at the next stage of the cascade. Figs. 6 and 8 plot the power available at each frequency in the cascade process for three different values of the starting power, $P_{\rm in}$, for our PhC and ring cavity designs. The figures also plot the corresponding intra-cavity energy in the fundamental and second-harmonic modes. The parameters corresponding to optimum performance are listed in Table I for the PhC designs and Table II for ring resonators (corresponding to the results in Fig. 8). The listed material properties ($\chi^{(2)}_{\rm eff}$ and n_a) are found in Appendix B and the cavity parameters ($Q^r_{a(b)}$, $Q^m_{a(b)}$, and $\tilde{\beta}$) are found in Appendix C. The coupling quality factors, $Q^c_{a(b)}$, are found by maximizing the absolute conversion efficiency as described above.

1. Nonlinear FDTD simulation

To verify and confirm our analytical results, we numerically obtained the efficiencies with nonlinear FDTD simulation. For nonlinear (susceptibility) FDTD of high-Q devices, we need to drastically suppress the time step for the stability of the simulation [58]. Instead, we can use recently developed unconditionally stable nonlinear FDTD [59], but it requires smaller mesh size due to the slow convergence. This is extremely detrimental for our case due to small tip structures. In addition, to build up the field for the steady-state nonlinear response (SHG), we cannot extract the efficiency from the short time dynamics as linear device Q simulation. This also requires a huge time overhead ($\sim\times10$) in the simulation.

Despite the challenges in the divergence of nonlinear FDTD, we present the simulation result supporting our proposal, by highly damping the cavity design for the stability. Figure 7 plots the efficiency from nonlinear FDTD simulation overlaid with the expected efficiency of damped cavity using Eq. (1). Cavity quality factors are adjusted

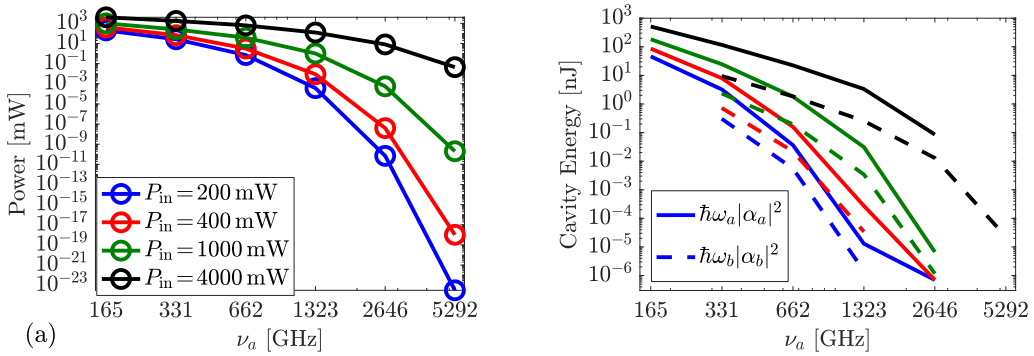

FIG. 6. Example of cascading using the best possible PhC design at each frequency. (a) Output power as a function of frequency for different input power. (b) Intra-cavity energy corresponding to the output powers in (a). Solid and dashed lines plot the energy in the fundamental and SH modes, respectively. Simulation parameters are listed in Table I.

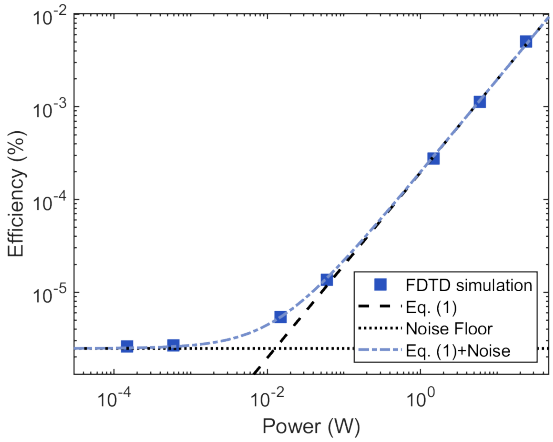

FIG. 7. Nonlinear FDTD simulation with highly damped cavity for stability. $Q_1 = 1,660$, $Q_2 = 133$, $f = 332$ GHz, and $LiNbO_3$ is used as a nonlinear material. For simplicity, we ignored waveguide coupling efficiency, i.e. $\eta = 1$, and collected radiated power from the structure. Note that $Q_{2,\mathrm{rad}} = 10,220$, but $Q_2 = [(1/Q_{2,\mathrm{rad}})^2 + (2\delta/\omega)^2]^{-1/2}$ was used for the inclusion of detuning. See Eq. (A7, 8) for the full equation of efficiency with detunings. The damping is achieved by removing holes, and the fundamental and second harmonic modes are damped differently due to the tighter mode confinement of the second harmonic mode. Note that at low power, data points deviate from Eq. (1) due to the simulation noise floor from the fundamental resonance frequency tail.

by decreasing the number of holes. Resulting Qs are $Q_1 = 1,660$, $Q_2 = 133$, $f = 332$ GHz. The Q of the SH mode was $Q_{2,\mathrm{rad}} = 10,220$, but $Q_2 = [(1/Q_{2,\mathrm{rad}})^2 + (2\delta/\omega)^2]^{-1/2}$ was adjusted for the inclusion of resonance detuning (see Eq. (A7, 8) for the treatment off detuning). Note that SH mode was barely damped due to tighter mode confinement, but adjusted using the detuning. Equation (1) has excellent agreement with the numerical simulation, verifying the validity of the theoretical analysis. At lower powers, simulation noise floor from the resonance tail pins the SHG efficiency.

2. Radiation loss by SH polarization

We estimate the conversion efficiency from the coupling of an induced SH polarization to the SH cavity mode. Analogous to spontaneous emission of an atom in cavity-QED, the SH polarization can directly radiate into free-space. To the best of our knowledge, this direct SH radiation has never been studied in the literature. We neglected this loss mechanism in our estimation and leave a quantitative analysis for future studies, but the discussion below briefly outlines how it should be incorporated.

The SH polarization field is driven by a source with a spatial distribution determined by $\vec{E}_a^2(\vec{r})$ and its amplitude is proportional to α_a^2. From the equation of motion of the fundamental field amplitude, α_a, Eq. (A5a), we know that the rate of change of α_a originating from its coupling to modes at $2\omega_a$ is proportional to $g\alpha_a^*\alpha_m$, where α_m is the

amplitude of the mth (leaky) mode at $2\omega_a$. Since the source of these modes is the SH polarization field, we have $\alpha_m \propto \alpha_a^2$, which results in a loss term in Eq. (A5a) proportional to $|\alpha_a|^2$

$$\frac{d\alpha_a}{dt} = [-i\delta_a - \kappa_a - \kappa_m|\alpha_a|^2]\alpha_a - i2g\alpha_a^*\alpha_b + i\sqrt{2\kappa_a^c}\epsilon_p, \tag{A11}$$

where the proportionality factor is denoted by κ_m. This term is analogous to two-photon absorption of the nonlinear medium. Due to the technical subtlety of determining κ_m, we leave it for future research. Nevertheless, this additional term can be neglected in the non-depleted regime. Thus, all the conversion efficiencies in %/W are unaffected by this term.

Freq. [GHz]	**Material**	$\boldsymbol{\chi_{\text{eff}}^{(2)}}$ **[m/V]**	$\tilde{\boldsymbol{\beta}}$	$\boldsymbol{Q_a^r}$	$\boldsymbol{Q_a^m}$	$\boldsymbol{Q_a^c}$	$\boldsymbol{Q_b^r}$	$\boldsymbol{Q_b^m}$	$\boldsymbol{Q_b^c}$	$\boldsymbol{n_a}$
165.4	$LiTaO_3$	2.46×10^{-8}	6.26×10^{-6}	3.58×10^{5}	2.06×10^{6}	1.8×10^{5}	4.16×10^{4}	6.14×10^{5}	1.9×10^{4}	6.13
330.7	$LiTaO_3$	2.49×10^{-8}	3.72×10^{-6}	3.58×10^{5}	1.05×10^{6}	2.3×10^{5}	4.16×10^{4}	3.10×10^{5}	2.5×10^{4}	6.14
661.5	$LiTaO_3$	2.62×10^{-8}	2.20×10^{-6}	3.58×10^{5}	5.16×10^{5}	2.0×10^{5}	4.16×10^{4}	1.42×10^{5}	2.9×10^{4}	6.17
1323	$LiNbO_3$	1.55×10^{-8}	1.71×10^{-6}	3.58×10^{5}	8.84×10^{5}	2.7×10^{5}	4.16×10^{4}	2.12×10^{5}	3.5×10^{4}	5.16
2646	$LiNbO_3$	3.02×10^{-8}	9.56×10^{-7}	3.58×10^{5}	3.53×10^{5}	1.9×10^{5}	4.16×10^{4}	2.85×10^{4}	1.7×10^{4}	5.37

TABLE I. Parameters used to calculate the cascaded output power for the PhC cavity design in Fig. 6 using a starting input power of $P_{\text{in}} = 1000\,\text{mW}$.

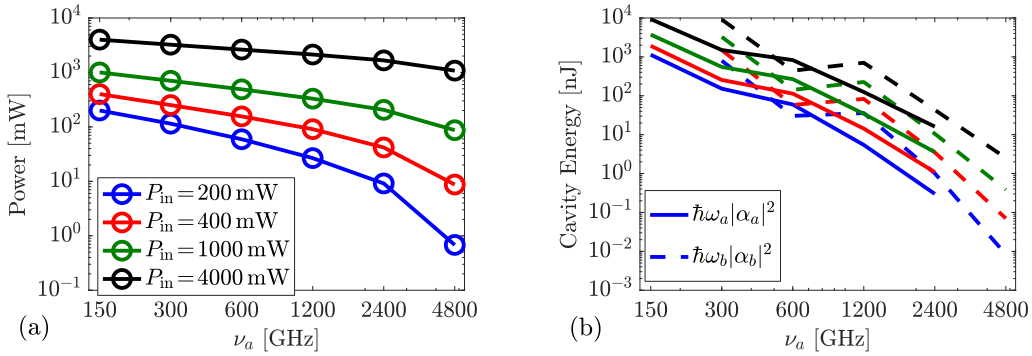

FIG. 8. Example of cascading using the best possible ring design at each frequency. (a) Output power as a function of frequency for different input power. (b) Intra-cavity energy corresponding to the output powers in (a). Solid and dashed lines plot the energy in the fundamental and SH modes, respectively. Simulation parameters are listed in Table II.

Freq. [GHz]	**Material**	$\boldsymbol{\chi_{\text{eff}}^{(2)}}$ **[m/V]**	$\tilde{\boldsymbol{\beta}}$	$\boldsymbol{Q_a^r}$	$\boldsymbol{Q_a^m}$	$\boldsymbol{Q_a^c}$	$\boldsymbol{Q_b^r}$	$\boldsymbol{Q_b^m}$	$\boldsymbol{Q_b^c}$	$\boldsymbol{n_a}$
175	$LiNbO_3$	1.3×10^{-8}	3.7×10^{-8}	2.4×10^{7}	1.1×10^{8}	4.0×10^{6}	2.7×10^{14}	8.2×10^{7}	1.0×10^{7}	5.10
350	$LiNbO_3$	1.3×10^{-8}	1.4×10^{-7}	1.9×10^{7}	1.3×10^{7}	1.7×10^{6}	1.8×10^{14}	1.0×10^{7}	1.3×10^{6}	5.10
700	GaP	1.1×10^{-10}	6.8×10^{-6}	1.3×10^{7}	5.5×10^{7}	2.4×10^{6}	8.2×10^{13}	4.3×10^{7}	6.1×10^{6}	3.32
1400	GaP	1.2×10^{-10}	2.4×10^{-5}	6.0×10^{6}	7.3×10^{6}	1.0×10^{6}	2.0×10^{13}	5.5×10^{6}	1.1×10^{6}	3.32
2800	GaP	1.5×10^{-10}	7.2×10^{-5}	2.0×10^{6}	9.8×10^{5}	3.4×10^{5}	2.4×10^{12}	5.6×10^{5}	2.0×10^{5}	3.34

TABLE II. Parameters used to calculate the cascaded output power for the ring cavity design in Fig. 8 using a starting input power of $P_{\text{in}} = 1000\,\text{mW}$.

Appendix B: Nonlinear material analysis

We consider nonlinear optical susceptibilities in the frequency region near phonon polariton resonances (termed the Reststrahl band). The coupling of a photon to a transverse optical (TO) phonon at frequency ω_{TO} in the THz or mid-IR yields the polariton dispersion relation and corresponding (linear) permittivity. Due to the shortage of high-power CW laser sources in the THz gap, however, there are few reports found in the literature of experiments measuring

nonlinear optical susceptibilities near the Reststrahl region. As noted in Ref. [60], which reported SHG experiments near the Reststrahl region of SiC, the few existing experimental studies [25, 26, 60–62] are limited. Therefore, we rely on a theoretical model to estimate the nonlinear susceptibilities, but emphasize that further experiments are needed.

A harmonic oscillator-based model of the $\chi^{(2)}$ nonlinear susceptibility in the Reststrahl region of crystalline materials was developed by Garrett [24]. Rather than electronic polarization, the dominant contribution in the region of polaritons comes from the transverse displacements of atoms in the lattice, which introduces a second, ionic, coordinate into the Lorentzian oscillator model [24]. Garrett considered the "anharmonic vibronic oscillator", an extension of the electronic oscillator model used to calculate higher order susceptibilities by perturbation theory, and derived a generalized Miller's Rule for nonlinear susceptibilities when both electronic polarization and lattice deformation are taken into account. Faust and Henry carried out early THz difference frequency generation experiments in GaP and fit the data to an anharmonic oscillator model of the $\chi^{(2)}$ for III-V semiconductors [27]. Mayer and Keilmann used these models to analyze THz SHG experiments in GaAs and $LiTaO_3$ [26]. Here we use Garrett's generalized Miller's Rule for the ferroelectric materials ($LiTaO_3$ and $LiNbO_3$) and the Faust-Henry model for the zincblendes (GaAs, GaP, ZnTe). We briefly describe them below.

The Lorentzian oscillator model describes the relative permittivity $\epsilon = (n - ic\alpha/2\omega)^2$,

$$\epsilon = \epsilon_\infty + \sum_j \frac{S_j \omega_{j\mathrm{TO}}^2}{\omega_{j\mathrm{TO}}^2 - \omega^2 + i\gamma_{j\mathrm{TO}}\omega}, \tag{B1}$$

where ω_{jTO} is the resonant frequency of the jth transverse optical phonon, γ_{jTO} is the linewidth of the resonance, S_j is the strength of the oscillator, and ϵ_∞ is the high frequency limit of the permittivity. Parameters used for each material are listed in Table III.

Perturbation theory relates the second order nonlinear susceptibility to the first order susceptibilities according to the anharmonic oscillator model [21]. Miller observed empirically that the ratio between the second order susceptibility and the products of the first order susceptibilities, often denoted as Miller's δ coefficient, remains relatively constant across materials and frequencies [63]. Garrett extended the description into the frequency range near vibrational modes, to include both electronic and ionic contributions to the $\chi^{(2)}$ via a sum of terms [24]:

$$\chi^{(2)}_{jkl}(\omega_1, \omega_2, \omega_3) = \sum_{abc} \delta^{abc}_{jkl} \chi^a_j(\omega_1) \chi^b_k(\omega_2) \chi^c_l(\omega_3), \tag{B2}$$

where the δ^{abc}_{jkl}'s are generalized Miller's δ's, the labels a, b, c are either i (referring to the ionic coordinate) or e (referring to the electronic coordinate), and the tensor component of the second order susceptibility is indexed by jkl. The $\chi^{a,b,c}_{j,k,l}$ are the *linear* susceptibilities at the associated frequencies.

When all three frequencies involved in the interaction are in the vicinity of TO phonon resonances, that is, $\omega_{1,2,3} \sim \omega_{\mathrm{TO}}$, the denominator of Eq. (B1) is resonant and we can make the approximation $\chi^i \gg \chi^e$. Further assuming that the δ^{abc}_{jkl}'s are comparable in magnitude (which is typically within reason), we can retain just the last term [24]

$$\chi^{(2)}_{jkl}(\omega_3, \omega_2, \omega_1) = \delta^{iii}_{jkl} \chi^i_j(\omega_3) \chi^i_k(\omega_2) \chi^i_l(\omega_1), \tag{B3}$$

where χ^i is calculated using Eq. (B1) with $\chi^i = \epsilon - 1$ (ordinary or extraordinary permittivity is chosen depending on the relevant tensor component). Comparison with the expression above for permittivity shows that the $\chi^{(2)}$ is a product of oscillator terms which retains its resonant features. For $LiTaO_3$ and $LiNbO_3$, which have high permittivities even at frequencies well below the TO phonon resonances ($\epsilon = 37.6$ and 26.0 along the c-axis, respectively [31, 32]) the approximation can still be made. (In general, however, all the terms in the sum must be considered). As reported values are lacking for δ^{iii}_{311} and δ^{iii}_{333} of $LiNbO_3$, and δ^{iii}_{333} of $LiTaO_3$, we assume that as the frequencies approach the microwave limit, the susceptibilities should approach the experimental microwave values, and we use these to fit the δ's [36]. With this fit, we obtain $\delta^{iii}_{31} = 25 \times 10^{-14}$ m/V for $LiTaO_3$, which we compare to $\delta^{iii}_{31} = 8 \times 10^{-14}$ m/V reported in Ref. [26]. Additionally, we find $\delta^{iii}_{33} = 50 \times 10^{-14}$ m/V for $LiTaO_3$, $\delta^{iii}_{31} = 36 \times 10^{-14}$ m/V and $\delta^{iii}_{33} = 85 \times 10^{-14}$ m/V for $LiNbO_3$.

In the zincblende crystals (GaAs, GaP, ZnTe), the dispersion of $\chi^{(2)}$ is instead described by the Faust-Henry model [27]:

$$\begin{aligned}\chi^{(2)}(\omega_3, \omega_2, \omega_1) = \chi^{(2)}_E \Bigg[& 1 + C_1 \left(\frac{1}{D(\omega_1)} + \frac{1}{D(\omega_2)} + \frac{1}{D(\omega_3)} \right) \\ & + C_2 \left(\frac{1}{D(\omega_1)D(\omega_2)} + \frac{1}{D(\omega_1)D(\omega_3)} + \frac{1}{D(\omega_2)D(\omega_3)} \right) + C_3 \frac{1}{D(\omega_1)D(\omega_2)D(\omega_3)} \Bigg]\end{aligned} \tag{B4}$$

where $\chi_E^{(2)}$ is the electronic nonlinear susceptibility, $C_{1,2,3}$ are the Faust-Henry coefficients, and $D(\omega) = 1 - (\omega/\omega_{\rm TO})^2 - i\gamma_{\rm TO}\omega/\omega_{\rm TO}^2$. The C_1 term accounts for interactions with one frequency near the TO phonon resonance, the C_2 term for interactions with two frequencies nearby, and the C_3 term accounts for all three contributions near the phonon resonance. Values (where available in the literature) can be found in Table IV.

Material	**Pol.**	ϵ_∞	$\Delta\epsilon$	ω_{TO} **(THz)**	γ_{TO} **(THz)**	**Ref(s).**
GaAs	-	11.55	1.95	8.05	0.29	Refs. [25, 26]
GaP	-	9.09	1.92	10.94	0.11	[27, 28]
ZnTe	-	3.0	6.92	5.3	0.09	[29, 30]
$LiTaO_3$	ord	7.73	24.10	4.26	0.42	[31]
			2.40	7.59	0.27	
			2.50	9.47	0.42	
			2.00	11.24	0.78	
			0.03	13.85	0.18	
			2.33	17.81	0.96	
	ext	6.78	30.00	6.00	0.84	[31]
			0.005	10.70	0.33	
			2.66	17.87	0.54	
			0.34	19.70	1.68	
$LiNbO_3$	ord	5.02	22.0	4.56	0.42	[32]
			0.80	7.08	0.36	
			5.50	7.94	0.36	
			2.20	9.65	0.33	
			2.30	10.88	0.99	
			0.18	12.92	0.36	
			3.30	17.57	1.05	
			0.20	20.09	1.41	
	ext	6.16	16.00	7.44	0.63	[32]
			1.00	8.21	0.42	
			0.16	9.20	0.75	
			2.55	18.83	1.02	

TABLE III. Parameters used to calculate THz refractive indices and absorption coefficients in Fig. 2 of the main text.

Material	$\chi_E^{(2)}$ (pm/V)	C_1	C_2	C_3	**Ref.**
GaAs	268	-0.59	0.14	-0.07	[25]
GaP	156	-0.53	-	-	[27]
ZnTe	139	-0.07	-	-	[29]

TABLE IV. Parameters used to calculate second-order nonlinear susceptibility of the zincblende materials, where available.

Appendix C: Cavity designs

1. PhC cavities

Photonic crystal cavities have two advantages in SHG: 1) they have a small mode volume resulting in increased energy density (SHG is proportional to the intensity squared); 2) they are phase-matching insensitive because the nonlinear material is only at the center. However, it is often very hard to obtain the energy matching condition ($\omega_b = 2\omega_a$) with PhC cavities. In this section, we show a systematic design approach for doubly resonant PhC cavities.

For a dielectric defect cavity, where the defect pulls down the air-like mode into the bandgap, often there are higher-order localized modes. We assume the following general situation; we have an initial cavity design with two low-Q cavity modes; they are near second-harmonic, $\omega_b = 2\omega_a + \delta$, but with large detuning, $\delta > \kappa_a, \kappa_b$. In this case, the conversion efficiency is small due to small Q-factors and large detuning. The goal of our design is to 1) increase Q_a and 2) Q_b and to 3) reduce the detuning, $\delta \ll \kappa_a, \kappa_b$. A direct optimization of three conditions requires the exploration of a full parameter space, which is time-intensive.

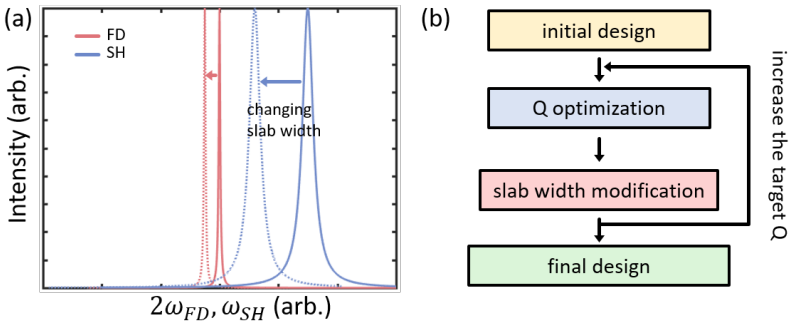

FIG. 9. A design flow for doubly resonant photonic crystal cavity. (a) The effect of changing the slab width. Solid lines represent the original cavity and dashed lines represent the resulting spectra after changing the slab width. (b) Flow chart describing our design algorithm. We first make an initial design that has two resonances with $\omega_b \approx 2\omega_a$, but with $\omega_b - 2\omega_a$ being larger than the resonance linewidth. We then alternate between Q-optimization and slab width modification. At each iteration, we increase the target Q while gradually approaching the resonance condition $\omega_b = 2\omega_a$.

Alternatively, we decoupled the optimization of the three conditions by separating the parameter space into three. The separation was chosen to be only sensitive to the corresponding condition to be optimized. More specifically, we optimized Q_b by changing the radii and positions of the first seven holes on each side of the center hole with the tips. On the other hand, optimization of Q_a happens through changing the outer twenty-five holes. Out of the twenty-five, the latter five have the radii and distances fixed to form Bragg mirrors. Our rationale for the choice of separation is that the fundamental mode is less tightly confined than the second-harmonic one. Thus, the optimization of the fundamental mode minimally affects the second-harmonic mode.

On the other hand, we adjust the detuning, $\delta = \omega_b - 2\omega_a$, with the slab width (Fig. 9). The second-harmonic mode we chose is the third order waveguide mode in the slab-width direction (for the mode anti-node to be located at the tip). Comparing with the fundamental mode (the first order waveguide mode), the second-harmonic mode is more tightly confined in the transversal direction (larger transverse k-vector). Thus, the resonant frequency of the second-harmonic mode is more sensitive to the slab width.

Our optimization process is summarized in Fig. 9(b). We perform the three optimizations and iterate. Starting with the initial design, Q_a and Q_b are optimized sequentially. When the target Q-factors are achieved, the width of the slab is adjusted to reduce the detuning. Despite separating the parameter space to minimize the coupling between parameters, the modification of the slab width reduces the Qs. We then increase the target Qs and iterate the optimization. When the Qs exceed the target value, we finalize the design.

2. PhC cavity simulations

We simulated PhC cavities with finite-difference time-domain (FDTD) method using a commercial software, Lumerical. We simulated a cavity at 331 GHz (fundmental) and 662 GHz (second-harmonic) and used Q and scaled mode field profiles at other frequencies (Maxwell's equations have scale invariance). The mode field profiles are obtained with $LiNbO_3$ as a nonlinear material ($n = 5.102$) at the center.

We used (15 μm×15 μm×20 μm) mesh and overrode the tip area (100 μm×100 μm×139 μm) with a mesh having a resolution of 500 nm×500 nm×10 μm. The cavity is first excited with a dipole, and the target modes are extracted using a standard mode profile monitor. We used the extracted mode for subsequent simulations for fast convergence and accurate parameter extraction. The quality factors of cavities are deduced from the decay rate of the electric field envelope (high-Q analysis).

3. Ring cavities

Phase-matching. Maximizing the conversion efficiency requires the ring to be both phase-matched and doubly resonant at the fundamental and SH frequencies. For two resonant frequencies of the ring, $\omega_{a(b)}$, the resonance condition is $\omega_{a(b)} = \frac{m_{a(b)}c}{Rn_{\text{eff}}(\omega_{a(b)},R)}$, where $m_{a(b)}$ is an integer that enumerates the azimuthal modes, $n_{\text{eff}}(\omega_{a(b)}, R)$ is the effective index of the waveguide, and R is the radius. With $\omega_b = 2\omega_a$, the phase-matching requirement $m_b = 2m_a$ is satisfied when $n_{\text{eff}}(\omega_a, R) = n_{\text{eff}}(2\omega_a, R)$. Using a finite difference eigenmode solver, we compute the effective indices

of the fundamental and second harmonic modes as a function of ω_a and R. The waveguide parameters are adjusted such that the effective index of the fundamental and SH modes are equal at a crossover frequency $\omega_a = \omega_{\text{cx}}$, shown in Fig. 10(a) for $LiNbO_3$ near 350 GHz. As the bending radius is reduced, the crossover frequency ω_{cx} increases, as plotted in Fig. 10(b). Where ω_{cx} intersects with one of the ring resonances (colored lines in Fig. 10(b)), the ring is simultaneously doubly resonant and phase-matched. Assuming the crossover frequency and effective index are well-behaved functions, they can be interpolated to find appropriate radii for ring resonance. For simplicity, in the main text we use a straight waveguide to approximate the efficiencies; however, with this method we confirm that the mode profiles and parameters are comparable to the bent waveguide case, and in principle can be used to phase match for a desired material and waveguide design.

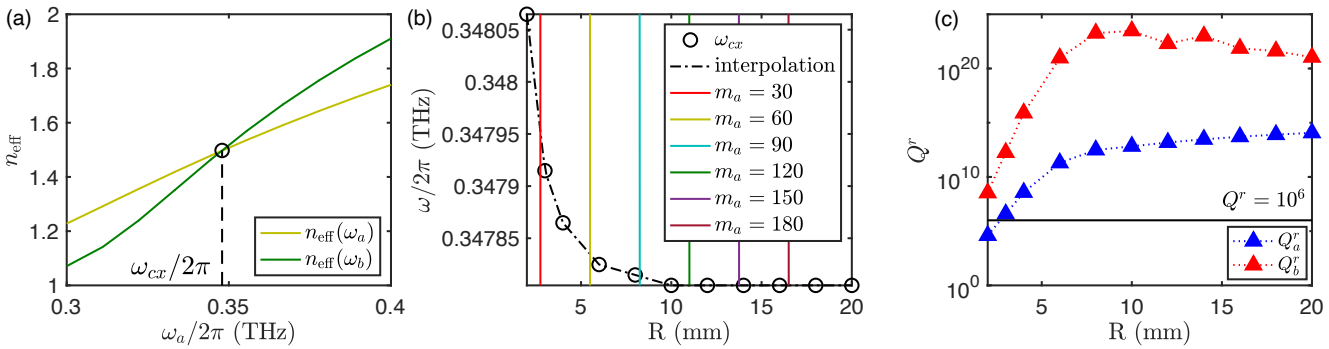

FIG. 10. Phase matching and radiation quality factor of the ring. (a) Effective index curves for fundamental and second harmonic modes of $LiNbO_3$ ring cavity with 100 nm × 100 nm tip area, shown for an example radius of 3 mm. (b) Waveguide n_{eff} crossover frequency plotted against radius and ring resonant frequencies with associated radius and n_{eff} for several integer values of m_a. Intersections of the colored curves with ω_{cx} give parameters at which the ring is phase matched ($n_{\text{eff}}(\omega_a) = n_{\text{eff}}(2\omega_a)$) and resonant at both ω_a and $2\omega_a$. (c) $Q^r_{a(b)}$ due to bending loss calculated for different R.

Radiation quality factor. Radiation loss limits the ring radius. To account for radiation losses due to bending of the ring, we calculated the radiation quality factor $Q^r_{a(b)}$ from the imaginary part of the modal effective index. Fig. 10(c) shows the minimum radius that is compatible with a radiation quality factor, $Q^r_{a(b)} \geq 10^6$. Considering this and the phase-matching condition, we choose a radius of $R = 3.2$ mm.

Material quality factor. To calculate the material quality factor $Q^m_{a(b)}$, we treated the absorption due to a small region of lossy nonlinear material as an imaginary perturbation to the dielectric function (see Appendix C 5 for details). The material quality factor is given by $Q^m_{a(b)} = \frac{\omega}{2\tilde{\kappa}^m_{a(b)}} = \frac{\epsilon'_{a(b)}}{\sigma_{a(b)}\epsilon''_{a(b)}}$ where the real and imaginary parts of the relative permittivity $\epsilon_{a(b)} = \epsilon'_{a(b)} + i\epsilon''_{a(b)}$ are given by the Lorentz oscillator model described in the main text, and $\sigma_{a(b)}$ is an overlap integral defined in Eq. (C5).

In Fig. 4 of the main text, we assumed critical coupling, which maximizes the SHG efficiency in the nondepleted pump limit. The overall quality factor $1/Q_{a(b)} = 1/Q^c_{a(b)} + 1/Q^m_{a(b)} + 1/Q^r_{a(b)}$ was used to compute the SHG efficiency using Eq. (A9).

Nonlinear mode overlap. The SHG overlap $\tilde{\beta}$ can be approximated in the ring resonator by [54]

$$\tilde{\beta}^{ring} \approx \frac{1}{\sqrt{2\pi R}} \frac{\int \bar{\epsilon}(x,y) E^2_{a,y}(x,y) E^*_{b,y}(x,y) dxdy}{\int \epsilon_a(x,y) \left|\vec{E}_a(x,y)\right|^2 dxdy \sqrt{\int \epsilon_b(x,y) \left|\vec{E}_b(x,y)\right|^2 dxdy}} \sqrt{\frac{\lambda_a^3}{n_a^3}} \delta(m_b - 2m_a), \tag{C1}$$

where $\bar{\epsilon}(x,y)$ is a function that equals 1 inside the nonlinear material and 0 everywhere else, and we assume coupling of three TM modes (E field polarized in the y direction) by the $\chi^{(2)}_{33}$ component of the nonlinear material ($\chi^{(2)}_{\text{eff}} = \chi^{(2)}_{33}$). The SHG overlap is maximized when the phase matching condition $\delta(m_b - 2m_a)$ is satisfied (with δ denoting the Dirac delta function).

4. Ring cavity simulations

Mode field profiles of the ring resonator were computed using the commercial 2D Finite Difference Eigenmode (FDE) solver Lumerical MODE and the open-source software MPB. At $\omega_a/2\pi \approx 350$ GHz, the dimensions of the

ring resonator cross section as indicated in Fig. 3 of the main text are $w = 150\,\mu\text{m}$, $h_a = 30\,\mu\text{m}$, $h_b = 91.8\,\mu\text{m}$, $w_{br} = 20\,\mu\text{m}$, $w_{tip} = 625$ nm, and $h_{tip} = 625$ nm. For calculation of the efficiencies in Fig. 4, however, we used $w_{tip} = h_{tip} = 100$ nm across all frequencies, which is in principle achievable with standard photolithography while being large enough relative to the lattice constants to treat the material as a continuous medium.

Field profiles in Fig. 3(b) were obtained using MPB for a straight waveguide with a uniform mesh of 122 nm × 122 nm at 350 GHz across the entire simulation region and periodic boundary conditions. To resolve the smallest tip sizes without prohibitive memory requirements, however, nonuniform meshing was used (available in Lumerical MODE but not MPB). Therefore, all calculations in Figs. 3c-f and Fig. 4 were implemented in Lumerical by applying a nonuniform mesh across the simulation region to ensure sufficient resolution in the nonlinear tip (minimum mesh size of 5 nm × 5 nm at 350 GHz).

To calculate radiation losses (in Lumerical), a bending radius was applied and perfectly matched layer (PML) boundary conditions were used on the three outer sides of the ring cross section; the fourth side corresponding to the direction of the center used metal boundary conditions. The bounding box was chosen to be large enough for convergence of the radiation Q to eliminate artifacts due to the PML.

The integrals in the expressions for $\tilde{\beta}^{ring}$ and $\sigma_{a(b)}$ were numerically evaluated over the entire (2D) simulation region.

5. Material absorption

Let us assume that we have data for the material loss from a measurement of the decay of an electromagnetic field as it propagates through the material. We assume the experimental conditions are such that we may consider the field to be a plane wave that evolves as $\exp(ik_0\tilde{n}z - i\omega_0 t)$. Then, the complex refractive index is defined as

$$\tilde{n} \equiv n + in'' \equiv \sqrt{\epsilon' + i\epsilon''} = \sqrt{\epsilon'}\sqrt{1 + \frac{\epsilon''}{\epsilon'}} \approx \sqrt{\epsilon'}\left(1 + i\frac{\epsilon''}{2\epsilon'}\right) \Rightarrow$$
$$n = \sqrt{\epsilon'}, \quad \text{and} \quad n'' = \frac{\epsilon''}{2n}, \tag{C2}$$

where we assumed $\epsilon' \gg \epsilon''$. The intensity absorption coefficient is

$$\alpha \equiv 2k_0 n'' = \frac{\omega_0}{c}\frac{\epsilon''}{n}, \tag{C3}$$

where $k_0 = \omega_0/c$ is the free-space wave number. If the intensity of the wave propagates at the group velocity and decays with the amplitude decay rate κ, then we have

$$\kappa \equiv \frac{1}{2}\alpha v_g = \frac{1}{2}\omega_0\frac{\epsilon''}{n_g n} \approx \frac{1}{2}\omega_0\frac{\epsilon''}{\epsilon'}. \tag{C4}$$

We set $n_g \approx n$ in Eq. (C4) since we assume the experiment was performed with an approximately plane wave propagating in a uniform material.

The contribution to material absorption from the nonlinear material inside our hybrid cavity designs are found [8, 55]

$$\tilde{\epsilon}''_{a(b)} = \epsilon''_{a(b)}\frac{\int dV\bar{\epsilon}(\boldsymbol{r})|\vec{E}_{a(b)}(\vec{r})|^2}{\int dV\epsilon(\boldsymbol{r})|\vec{E}_{a(b)}(\vec{r})|^2} \equiv \epsilon''_{a(b)}\sigma_{a(b)} \;\Rightarrow\; \tilde{\kappa}^m_{a(b)} \equiv \kappa^m_{a(b)}\sigma_{a(b)}, \tag{C5}$$

where $\bar{\epsilon}(\boldsymbol{r})$ is a function that equals 1 inside the nonlinear material and 0 everywhere else. Here, we denoted the effective decay rate using a $\tilde{}$ and Eq. (C5) shows that the bulk decay rate, $\kappa^m_{a(b)}$, is reduced by a factor of $\sigma_{a(b)}$. Note, however, that elsewhere in the manuscript we use $\kappa^m_{a(b)}$ to denote the effective decay rate for notational convenience.

6. Material loss of host cavities

Here we discuss the material losses in the host cavities. While we assumed lossless silicon in the calculations, high-resistivity float-zone silicon (HRS) is a realistic candidate for the low-loss dielectric material [64]. HRS is one of the conventionally used materials for THz and mm-wave applications because of its low absorption. Using the Drude model, 400 kΩ cm Si [65, 66] has material quality factors $Q \sim 4 \times 10^5$ at 150 GHz and $Q \geq 1 \times 10^6$ above ∼300 GHz (Fig. 11). We expect that an improvement by a factor of ∼20 in the resistivity of silicon would make it effectively lossless in all calculations, with $Q > 10^7$.

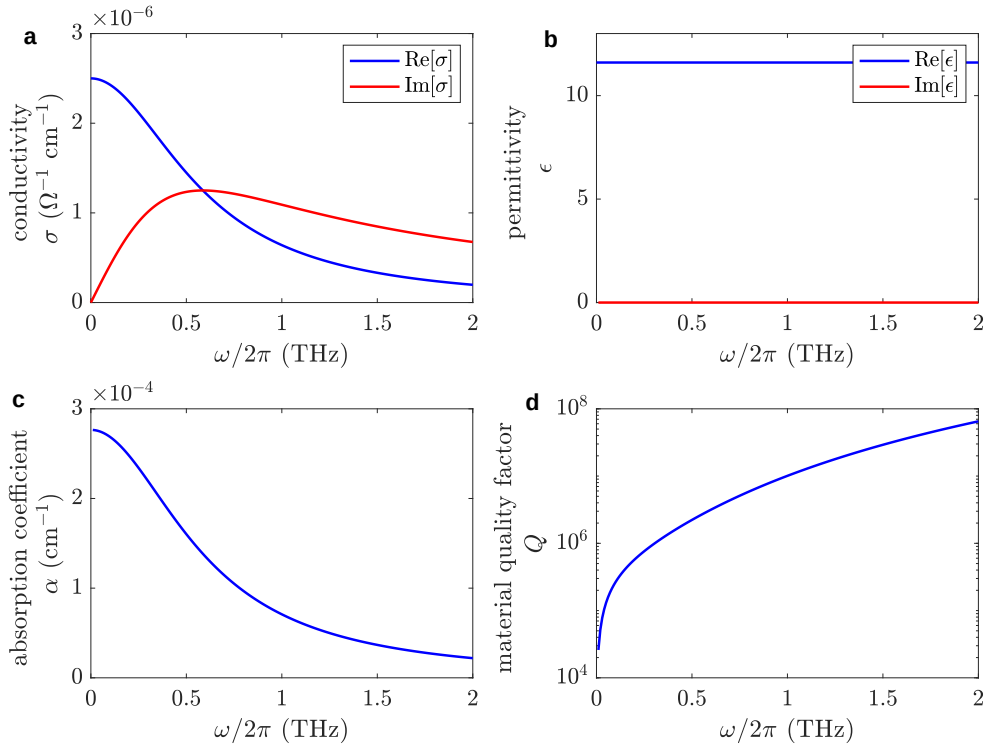

FIG. 11. High-resistivity Si Thz characteristics with Drude model. (a) Conductivity, (b) permittivity, (c) absorption coefficient, and (d) material quality factor.

Appendix D: Dielectric Breakdown

Due to the strong field confinement of our cavity designs, it is important to consider the limitations imposed by dielectric breakdown. To evaluate the field strength in the cavities, we re-normalize the eigenmodes as

$$\vec{\mathcal{E}}_n(\vec{r}) \equiv \vec{E}_n(\vec{r}) \sqrt{\frac{\hbar\omega_n|\alpha_n|^2}{\int \epsilon_0\epsilon(\vec{r})|\vec{E}_n(\vec{r})|^2 dV}}, \tag{D1}$$

where $\hbar\omega_n|\alpha_n|^2$ is the energy in cavity mode n found from Eq. (A5). This re-normalized field correctly accounts for the electromagnetic energy in the cavity

$$\int \epsilon_0\epsilon(\vec{r})|\vec{\mathcal{E}}_n(\vec{r})|^2 dV = \hbar\omega_n|\alpha_n|^2, \tag{D2}$$

and therefore provides the electric field in SI units of V/m. Comparison of the maximum electric field in each cavity material with the dielectric strength of the corresponding material provides the limit on the input power given by dielectric breakdown.

Figures 12 and 13 plot the maximum field strength in V/m for the PhC and ring, respectively, corresponding to the intra-cavity energies in Figs. 6 and 8 for P_{in} = 200 mW (blue), 400 mW (red), 1000 mW (green), and 4000 mW (black). Parts (b) indicate that the maximum electric field in the air near the tips exceeds the breakdown field of 3×10^6 V/m [67]; operating the device in vacuum would shift the consideration onto the waveguide materials. Figs. 12(a) and 13(a) show that the maximum electric field in the silicon peaks near 1×10^8 V/m in both the PhC and the ring, and that in the nonlinear material peaks near 6×10^7 V/m in the PhC (lithium niobate) and 1.5×10^8 V/m in the ring (gallium phosphide), for 4 W of input power at the seed oscillator. For comparison, gallium phospide exhibits a breakdown field of 1×10^8 V/m [68], while bulk lithium niobate can tolerate THz field strengths of over 1×10^8 V/m without breakdown [69], and possibly higher for the small tip gaps considered here. Silicon, on the other hand, has a theoretical intrinsic breakdown field of 8×10^7 V/m (independent of electrode separation), making it the limiting material in this case. Issues with dielectric breakdown can be circumvented by using materials with higher breakdown fields (e.g. diamond, with 2×10^9 V/m [70]), increasing the cavity size, and compensating losses

by coherently combining outputs between stages of the cascade. Such modifications could potentially allow operation at input powers exceeding 4 W, improving the overall cascaded conversion efficiency.

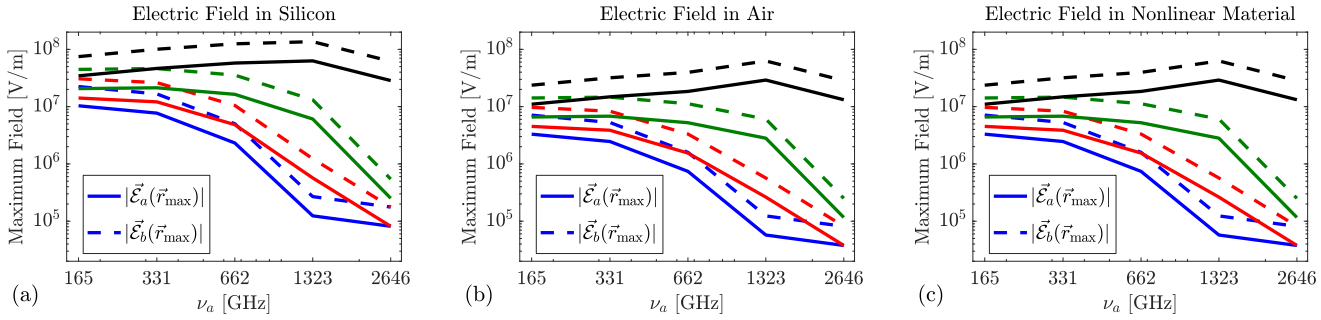

FIG. 12. Maximum field strength in each of the PhC cavity materials corresponding to the power and intra-cavity energy in Fig. 6.

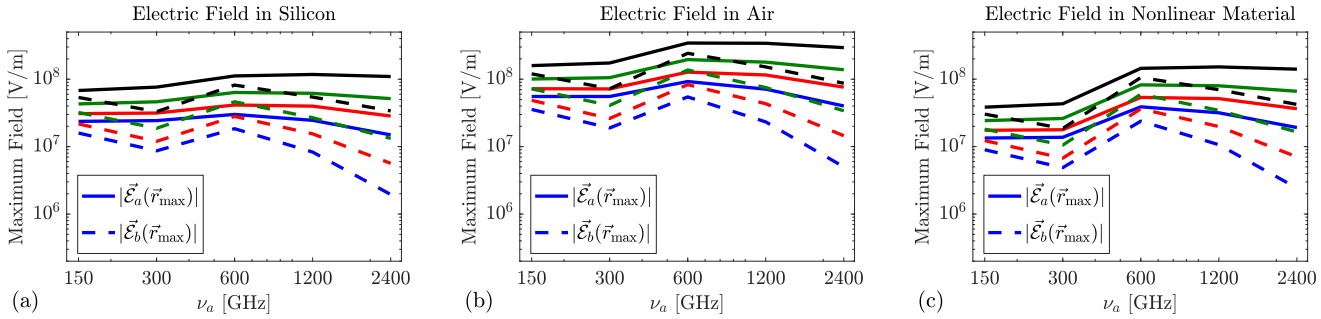

FIG. 13. Maximum field strength in each of the ring cavity materials corresponding to the power and intra-cavity energy in Fig. 8.

Appendix E: Back reflection

The back reflections in the coherent system can significantly affect the efficiencies. Though we analyze the back reflections below, we want to argue that back reflection can be readily suppressed with circulators [71] and isolators [72, 73]. With these devices, one can achieve < 2 dB insertion loss with > 20 dB isolation, which is enough for even poorly fabricated devices.

Next, we consider the effect of back reflection by imperfect critical coupling. If the optical path length between two subsequent stages are sufficiently large, we can assume the continuum mode limit. On the other hand, there will be Febry-Perot resonances for small optical path length. In this case, one can engineer the resonance for the efficiencies. However, we primarily focus on the former case since the additional mode engineering might be technologically challenging.

For the continuum intermediate mode, the input-output relation of the output field, Eq. (A5c) is modified;

$$\epsilon_{\mathrm{SHG}} = rI\epsilon_{\mathrm{SHG}} - \sqrt{2\kappa_b^c}\alpha_b \tag{E1}$$

where r is the reflection coefficient from the next stage, I is the isolation. Without loss of generality, we assume that r is real and $1 \geq r \geq 0$. Also, the SH equation of motion, Eq. (A5b) is changed to be,

$$\frac{d\alpha_b}{dt} = -\kappa_b\alpha_b - ig^*\alpha_a^2 + i\sqrt{2\kappa_b^c}\cdot rI\epsilon_{\mathrm{SHG}}, \tag{E2}$$

where we assumed $\delta_b = 0$ for simplicity. In the steady-state,

$$\alpha_b = \frac{-ig^*\alpha_a^2}{\kappa_b + i\frac{rI}{1-rI}\cdot 2\kappa_b^c}. \tag{E3}$$

Note that $\kappa_b \to \kappa_b + i\frac{rI}{1-rI} \cdot 2\kappa_b^c$ under the back reflection, and it does not affect in the limit $rI \to 0$. We can show the ratio of the intermediate output power with and without back reflection is,

$$f = \left| \frac{\epsilon_{\mathrm{SHG}}^{\mathrm{w}}}{\epsilon_{\mathrm{SHG}}^{\mathrm{w/o}}} \right|^2 = \left| \frac{1}{(1-rI)+irI} \right|. \tag{E4}$$

Note that as $rI \to 1$, $f \to 1$, but in this case all $\epsilon_{\mathrm{SHG}}^{\mathrm{w}}$ is fed back to the cavity and not usable in the next stage. Thus a fair value to be compared should be the injected power to the next stage,

$$(1-r^2)f = \frac{1-r^2}{1-2rI+2(rI)^2} \begin{cases} 1+2rI, & r \to 0 \\ 0, & r \to 1 \\ 1-r^2, & I \to 0 \\ (1-r^2)/(1-2r+2r^2), & I \to 1 \\ \approx 1.618. & (r,I) = (0.38, 1) \end{cases} \tag{E5}$$

Summarizing, when one can precisely control the devices, by setting $(r, I) = (0.38, 1)$, one can boost linear efficiency (%/W) by a factor of ≈ 1.618. Realistically, the phase coming from reflection and the propagation between stages is not controllable, high isolation ($I \to 0$) guarantees minimum efficiency reduced by the reflectance, i.e. by a factor of $(1-R)$. When the isolation is not available, the linear efficiency of the stage drops by a factor of $(1-2|r|) = (1-2\sqrt{R})$, for $r < 0, |r| \ll 1$. (Note that we assumed $1 \geq r \geq 0$, but in principle, r can have any phase that is uncontrollable.) Thus, the isolation quadratically suppress the back reflection.